



This discussion paper is/has been under review for the journal Nonlinear Processes in Geophysics (NPG). Please refer to the corresponding final paper in NPG if available.

Shoaling of internal solitary waves at the ASIAEX site in the South China Sea

K. G. Lamb¹ and A. Warn-Varnas^{2,*}

¹Department of Applied Mathematics, University of Waterloo, Waterloo, Ontario, N2L 3G1, Canada

²Naval Research Laboratory, Stennis Space Center, MS 39539, USA

*retired

Received: 8 June 2014 – Accepted: 24 June 2014 – Published: 31 July 2014

Correspondence to: K. G. Lamb (kglamb@uwaterloo.ca)

Published by Copernicus Publications on behalf of the European Geosciences Union & the American Geophysical Union.

Shoaling internal solitary waves

K. G. Lamb and
A. Warn-Varnas

Title Page

Abstract

Introduction

Conclusions

References

Tables

Figures



Back

Close

Full Screen / Esc

Printer-friendly Version

Interactive Discussion



Abstract

The interaction of barotropic tides with Luzon Strait topography generates westward propagating internal bores and solitary waves trains which eventually shoal and dissipate on the western side of the South China Sea. Two-dimensional numerical simulations of this shoaling process at the site of the Asian Seas International Acoustic Experiment (ASIAEX) have been undertaken in order to investigate the sensitivity of the shoaling process to the stratification and the underlying bathymetry, and to explore the influence of rotation. A range of wave amplitudes are considered. Comparisons with adiabatic shoaling waves are also made and the potential impact of a non-slip boundary condition are briefly explored. On the slope secondary solitary waves and mode-two wave packets are generated which propagate towards the shelf. Comparisons with observations made during the ASIAEX experiment are made.

1 Introduction

In the South China Sea (SCS) large internal solitary-like waves (ISWs) are frequently observed, both remotely via Synthetic Aperture Radar (SAR) and in situ (Liu et al., 1998; Ramp et al., 2004; Klymak et al., 2006; Farmer et al., 2009; Li and Farmer, 2011). Analysis of SAR surface signatures, and time series of current and temperature data at moorings, indicate that the ISWs are generated by barotropic tidal motion over the large sills in Luzon Strait and on the slope region of the northern boundary of the SCS (Liu et al., 1998; Hsu and Liu, 2000). Depressions generated in Luzon Strait propagate westwards across the deep South China Sea basin, where depths can exceed 4000 m, to the Asian Seas International Acoustic Experiment (ASIAEX) experimental site on the Chinese continental shelf. Nonlinear effects steepen these depressions until they disintegrate into ISWs of large amplitude, through frequency and amplitude dispersion. Zhao and Alford (1989) related the ISWs observed near Dongsha Island

NPGD

1, 1163–1222, 2014

Shoaling internal solitary waves

K. G. Lamb and
A. Warn-Varnas

Title Page

Abstract

Introduction

Conclusions

References

Tables

Figures



Back

Close

Full Screen / Esc

Printer-friendly Version

Interactive Discussion



to tidal currents passing through Luzon Strait, finding that westward flow through the strait was responsible for the generation of the ISW packets.

Li and Farmer (2011) reported deep basin ISW amplitudes as large as 150 m with typical values being around 50 m. In situ measurements in the deep basin by Klymak et al. (2006) show ISWs with amplitudes as large as 170 m and phase speeds of 2.9 m s^{-1} . During the joint Variations Around the Northern South China Sea (VANS) and Windy Island Soliton Experiment (WISE) (Yang et al., 2009), ISWs with amplitudes of up to 220 m and phase speeds of around 3.4 m s^{-1} (Ramp, private communication) were observed. These measured amplitudes and phase speeds are among the largest observed anywhere, surpassing observed amplitudes of 90 m and phase speeds of 1.8 m s^{-1} in the Andaman and Sulu Seas (Osborne and Burch, 1980; Apel et al., 1985). Because of the large amplitudes of these waves they have been the subject of many observational and numerical investigations. The dynamics of ISWs in the northern SCS was recently reviewed by Guo and Chen (2014).

Several numerical studies of ISW generation by tidal flow over the ridges in Luzon Strait have been conducted (Niwa and Hibiya, 2001, 2004; Warn-Varnas et al., 2010; Buijsman et al., 2010) elucidating the generation of ISWs in Luzon Strait and their subsequent westward propagation in the South China Sea. The structure of ISW wave trains in the SCS is variable with large amplitude wave trains separated by small amplitude wave trains (Ramp et al., 2004; Warn-Varnas et al., 2010; Buijsman et al., 2010; Vlasenko et al., 2012). Ramp et al. (2004) separated the wave packets observed at the ASIAEX site into *a* waves and *b* waves. The *a* waves arrived at regular 24 h intervals and were rank ordered, with the largest wave leading the wave packet. The weaker *b* waves were separated by approximately 25 h and were more irregular, with the largest wave usually in the middle of the packet.

During the ASIAEX experiment, intensive measurements of shoaling ISW trains over the continental shelf off China were undertaken (Lynch et al., 2004; Duda et al., 2004; Orr and Mignerey, 2003; Ramp et al., 2004). Ramp et al. (2004) reported on observations from a series of moorings spanning depths of 350 to 72 m. At 350 m depth wave

Shoaling internal solitary waves

K. G. Lamb and
A. Warn-Varnas

Title Page

Abstract

Introduction

Conclusions

References

Tables

Figures



Back

Close

Full Screen / Esc

Printer-friendly Version

Interactive Discussion



Shoaling internal solitary wavesK. G. Lamb and
A. Warn-Varnas

Title Page

Abstract

Introduction

Conclusions

References

Tables

Figures

◀

▶

◀

▶

Back

Close

Full Screen / Esc

Printer-friendly Version

Interactive Discussion



amplitudes ranged from 29 to 142 m (based on the displacement of the 24° isotherm). Their observations illustrated the evolution of these waves as they shoaled. At 350 m depth the waves were fairly symmetric. By the time they reached a depth of 200 m they had usually deformed significantly with a gently sloping front and a much steeper rear. Orr and Mignerey (2003) tracked a shoaling solitary wave train with a towed conductivity, temperature, and depth sensor (CTD), observing the evolution of shoaling ISW trains from waves of depression to waves of elevation.

Liu et al. (1998) demonstrated, with a two-layer Gardner equation (Kortweg-deVries extended to include a cubic nonlinear term) model that ISW depressions are transformed into a train of ISWs of elevation as they propagate over sloping topography into shallower water. Vlasenko and Stashchuk (2007) studied three-dimensional shoaling in the Andaman Sea with a fully nonlinear nonhydrostatic numerical model using a continuous stratification. Results showed the transformation of ISWs of depression to waves of elevation as well as refraction effects. Orr and Mignerey (2003) modeled a single shoaling soliton with the Gardner equation and showed a change from depression to elevation over their measurement slope.

The vast majority of observed nonlinear internal waves in the South China Sea are mode-one waves however several observations of mode-two waves have been made. During VANS/WISE mode-two waves were observed on the Chinese continental slope at 350 m depth where they appear to have been generated by shoaling mode-one ISWs (Yang et al., 2009, 2010).

The breaking of solitary waves travelling up slope has been addressed by several researchers. Helfrich and Melville (1986) and Helfrich (1992) considered the breaking criteria for a two-layered system. Vlasenko and Hutter (2002) performed simulations, in a continuously stratified fluid, of breaking solitary waves on slope-shelf topography and determined a parametrization for the location of wave breaking for stratifications and bathymetry based on observations in the Andaman and Sulu Seas.

In this study modeling of a shoaling solitary wave train is undertaken at the ASIAEX experimental site (Orr and Mignerey, 2003; Duda et al., 2004; Ramp et al., 2004). The

model, bathymetries and stratifications used in this study is described in Sect. 2. Results of the simulations are presented in Sect. 3 where sensitivity to the bathymetry, stratification, rotational effects and the potential implications of viscosity are considered. Comparisons with observations from the ASIAEX and conclusions are presented in Sect. 4.

2 Modelling

2.1 Numerical model

The two-dimensional fully nonhydrostatic Internal Gravity Wave model (Lamb, 1994, 2007) is used in this study of shoaling ISWs. Flow in the along shelf y -direction is included but the flow is independent of y . The model uses the rigid-lid, traditional f -plane, Boussinesq and incompressible flow approximations. The governing equations are

$$\mathbf{u}_t + \mathbf{u} \cdot \nabla \mathbf{u} - f \mathbf{u} \times \hat{k} = -\frac{1}{\rho_0} \nabla p - \frac{\rho}{\rho_0} g \hat{k} + \nabla \cdot (v \nabla \mathbf{u}), \quad (1a)$$

$$\rho_t + \mathbf{u} \cdot \nabla \rho = \nabla \cdot (v_r \nabla \rho), \quad (1b)$$

$$\nabla \cdot \mathbf{u} = 0, \quad (1c)$$

where z is the vertical coordinate, (x, y) are the horizontal coordinates directed across and along the topography, $\mathbf{u} = (u, v, w)$ is the velocity field with components in (x, y, z) directions, \hat{k} is the unit vector in the z -direction, ρ is the density, ρ_0 is the reference density, and p is the pressure. ∇ is the 3-D vector gradient operator, however all fields are independent of y . The subscript t denotes differentiation with respect to time. The gravitational acceleration is $g = 9.81 \text{ m s}^{-2}$ and for simulations including rotational effects the Coriolis parameter is $f = 5.33 \times 10^{-5} \text{ s}^{-1}$ corresponding to a latitude of 21.5° N. v and v_t are a spatially varying viscosity and diffusivity. Most of our simulations do not use explicit viscosity and diffusion terms, we return to this later. The model uses

Shoaling internal solitary waves

K. G. Lamb and
A. Warn-Varnas

Title Page

Abstract

Introduction

Conclusions

References

Tables

Figures

◀

▶

◀

▶

Back

Close

Full Screen / Esc

Printer-friendly Version

Interactive Discussion



behaviour will depend on the initial location of the ISW. We do not consider this. The initial waves are placed in the deep water. Because of the different lengths of the shelf slopes the initial location depends on the bathymetry: for bathymetries h_0 and h_{15} the waves are started at $x = -280$ and -200 km respectively.

2.4 Weakly-nonlinear theory and conjugate flow amplitudes

Weakly-nonlinear theory is often used to approximate observed internal solitary waves. Including cubic nonlinearity and ignoring damping and rotational effects, internal solitary waves in a fluid of constant depth can be modeled with the Gardner (or extended KdV) equation

$$\eta_t + c_0 \eta_x + \alpha \eta \eta_x + \alpha_1 \eta^2 \eta_x + \beta \eta_{xxx} = 0. \quad (2)$$

Ignoring the cubic nonlinear term (i.e. $\alpha_1 = 0$) results in the KdV equation. It predicts solitary waves of depression when $\alpha < 0$ and solitary waves of elevation when $\alpha > 0$. For our base stratification $\alpha < 0$ for depths greater than about 91.8 m and positive in shallower depths. When $\alpha_1 < 0$ solitary wave solutions of the Gardner equation have a limiting amplitude of $-\alpha/\alpha_1$ while for $\alpha_1 > 0$ solitary waves of depression and elevation exist. When $\alpha < 0$ waves of depression with any amplitude exist while waves of elevation exist with amplitudes greater than the minimum amplitude of $-2\alpha/\alpha_1$. The opposite is the case when $\alpha > 0$. Using α_1 to predict the existence of solitary waves with both polarities is problematic because α_1 is not uniquely determined (Lamb and Yan, 1996). Choosing α_1 so that the second-order vertical structure function for the isopycnal displacement is zero at the depth where the leading-order eigenfunction has its maximum is a common choice (Grimshaw et al., 2002). This choice for selecting α_1 predicts that solitary waves of either polarity exist in depths greater than 235 m using our base stratification. In shallower water it predicts that only waves of one polarity exist. Fully nonlinear ISWs generally have limiting amplitudes. As this amplitude is approached they broaden and become horizontally uniform in their centre. The flow state in the centre of these flat-crested waves is called a conjugate flow. We computed

Shoaling internal solitary waves

K. G. Lamb and
A. Warn-Varnas

Title Page

Abstract

Introduction

Conclusions

References

Tables

Figures



Back

Close

Full Screen / Esc

Printer-friendly Version

Interactive Discussion



Shoaling internal solitary waves

K. G. Lamb and
A. Warn-Varnas

Title Page	
Abstract	Introduction
Conclusions	References
Tables	Figures
◀	▶
◀	▶
Back	Close
Full Screen / Esc	
Printer-friendly Version	
Interactive Discussion	

conjugate flow solutions for depths between 50 and 400 m which provide the limiting asymptotic amplitude, propagation speeds and maximal currents for solitary waves (Lamb and Wan, 1998) as the wave energy goes to infinity. The amplitudes of these solutions for the base stratification $\bar{\rho}_b$ are shown in Fig. 4. Again, only single solutions were found (which vary almost linearly with depth). These solutions have the polarity predicted by the KdV equation.

Stratifications $\bar{\rho}_b$ and $\bar{\rho}_1$ have critical points, locations where α changes sign, at depths of about 91.8 and 120.0 m respectively: in greater depths ISWs are waves of depression while in shallower depths, in particular on the shelf, ISWs are waves of elevation. Thus for these two stratifications shoaling waves pass through a critical point on their way to the shelf which has significant implications for their evolution. Stratification $\bar{\rho}_2$, with its higher pycnocline, does not have a critical point.

We have used waves with several different amplitudes based on observed amplitudes (Ramp et al., 2004). The energies and wave amplitudes for several different initial waves are provided in Table 1.

3 Results

We begin by showing results for two simulations using an initial wave of amplitude 45.5 m with each of the bathymetries (Cases 2 and 3). Following this we explore sensitivity to resolution before discussing more fully the complete set of simulations.

Figure 5 shows results from a simulation using bathymetry h_0 and the base stratification $\bar{\rho}_b$ (Case 2). A small initial wave of amplitude 45.4 m is used in water 3000 m deep (APE 50 MJ m^{-1}). Figure 5a shows the full continental slope and the initial wave which is barely visible at $x = -280 \text{ km}$. After 25 h the leading wave is at $x = -64 \text{ km}$ where the water depth is about 650 m (Fig. 5b). A second solitary wave is visible approximately 15 km behind the leading wave. At $t = 42 \text{ h}$ (Fig. 5c) the leading wave, approximately 1.5 km in length, has reached a depth of 250 m at $x = 37 \text{ km}$. Three solitary waves are now visible. By $t = 50 \text{ h}$ (Fig. 5d) the leading wave has significantly deformed. It is now



Shoaling internal solitary waves

K. G. Lamb and
A. Warn-Varnas

Title Page

Abstract

Introduction

Conclusions

References

Tables

Figures



Back

Close

Full Screen / Esc

Printer-friendly Version

Interactive Discussion



about 3 km long and spans water depths of 130 to 140 m. The slope of the wave front is less that it was at $t = 42$ h and in the centre of the wave the slope of the thermocline is greatly reduced, being almost parallel with the bottom. This is a well know feature of shoaling waves when the thermocline is close to the bottom (Vlasenko and Hutter, 2002; Orr and Mignerey, 2003; Lamb and Nguyen, 2009). The rear of the wave is much steeper and behind the leading depression the thermocline has been raised above its equilibrium position. This we refer to as the wave pedestal. There are now three distinct waves of depression trailing the leading wave. As the wave continues to shoal and passes beyond the critical point at 91 m depth (Fig. 5e), the front part of the leading depression becomes very long with a very shallow slope. On the shelf solitary waves of depression in the ambient stratification do not exist so the leading depression gradually fades away losing energy to the trailing waves. The steep back of the wave never overturns and the second solitary wave, which has now propagated into the pedestal behind the leading wave, has the form of a square wave with the centre of the wave parallel to the bottom separating a very steep front and back (Fig. 5e). This wave is approximately at the critical point of the background stratification but it is propagating on the wave pedestal trailing the leading wave and this is the environment it propagates in. This environment consists of a background sheared flow with positive vorticity ($u_z > 0$) and a modified stratification. By $t = 66$ h the waves are on the shelf. Breaking has commenced behind the third depression.

Figure 6 shows a close up of the wave field and wave breaking at $t = 66$ h. Vertical profiles of the horizontal velocity and density in the wave depressions and wave pedestals at the locations indicated by the vertical dashed lines are shown in Fig. 7a and b. In the two wave depressions (profiles at $x = 94$ and 91 km) the horizontal velocities are similar. The second pedestal (at $x = 89$ km) has stronger currents that the first does ($x = 92$ km). Furthermore in the second pedestal the current at the bottom has a bulge with the maximum current of about 0.5 m s^{-1} occurring about 5 m above the bottom. This is equal to the estimated propagation speed of the rear of the second pedestal. The density profiles (Fig. 7b) show that in the second pedestal fluid in the

Shoaling internal solitary waves

K. G. Lamb and
A. Warn-Varnas

Title Page

Abstract

Introduction

Conclusions

References

Tables

Figures



Back

Close

Full Screen / Esc

Printer-friendly Version

Interactive Discussion



for bathymetry h_0 which is likely responsible for the two leading waves being closer together when bathymetry h_{15} is used. As a consequence, when the leading waves arrive on the shelf the wave pedestal between the leading and second waves of depression is much shorter for bathymetry h_{15} (500 m vs. 1500 m). In addition to the differences in the steepness of the shelf slope bathymetry h_{15} has a bump at a depth of about 700 m, much shallower than the bump in bathymetry h_0 . This bump modifies the wave field resulting in the generation of higher mode waves (Fig. 8b) as can be seen by the internal wave beam sloping up from the bump. A zoom in of the higher-mode waves at $t = 29$ h (same time shown in Fig. 8c) is shown in Fig. 9. Downwelling behind the bump after the wave has passed over it can be seen at $x \approx -15$ which can in some cases result in larger vertical excursions than in the leading wave. Breaking behind the shoaling waves commences earlier for the steeper bathymetry (compare Figs. 5e and 8e).

3.1 Resolution

It is important to have high enough resolution to adequately resolve solitary waves as they shoal. If the resolution is too low unphysical solitary-like waves can be simulated due to a balance between nonlinearity and numerical dispersion (Hodges et al., 2006; Vitousek and Fringer, 2011). Vitousek and Fringer (2011) considered waves propagating in a 2000 m deep domain using a stratification based on observations in the South China Sea and found that resolutions coarser than about 250 m resulted in waves that were two wide.

We have performed a number of resolution tests. In the first series of tests the horizontal resolution was varied ($\Delta x = 250, 100, 50$ and 33 m). In the first set an initial wave of amplitude 45 m shoaled from a depth of 3000 m using bathymetry h_{15} . The waves were started at $x = -200$ km. The maximum time steps were 12.5, 5.0, 2.5 and 2.5 s respectively and a vertical resolution of $J = 200$ was used. Results from the case with $\Delta x = 33$ m were shown in Fig. 8. Increasing the time step to 5.0 s in the $\Delta x = 50$ m simulation resulted in negligible differences. After traveling over 120 km to a depth of

2500 m the amplitudes in all four cases varied by about 2% with the wave amplitude increasing as the resolution increased. By the time the waves had travelled 180 km to a depth of 800 m, just before the bump, the solitary wave in the $\Delta x = 250$ m simulation was about 5% smaller than that in the highest resolution case. After this stage the solutions diverged more rapidly.

Figure 10 compares the surface currents $u(x, 0, t)$ at four different times when the leading wave is in water depths of 600, 395, 180 and 85 m. The first two panels compare results from the three coarsest resolutions, the results from the two finest resolved cases being nearly identical at these depths. At 180 m depth we only show results from the three finest resolutions. By the time the waves have reached a depth of 600 m (Fig. 10a) the leading wave has begun fissioning into several waves. The wave in the 250 m resolution case is significantly smaller than those in the other simulations. By the time the wave has reached a depth of 395 m (Fig. 10b) the amplitude of the leading wave in the 250 m resolution case is grossly underestimated and has the form of a small undular bore. In contrast in the higher resolution simulations two large leading solitary waves have emerged trailed by a train of smaller waves. The amplitude of the leading wave in the 100 m resolution simulation is now about 87% that of the highest resolution case. The result from the 50 m resolution simulation is indistinguishable from the 33 m resolution case at 600 and 395 m depths. By the time the waves have reached a depth of 180 m (Fig. 10c) the leading wave in the 100 m simulation has continued to decay relative to the higher resolution simulation. It now has an amplitude approximately 77% of that in the 33 m resolution case. Results from the 50 and 33 m resolution cases can now be distinguished, with the waves in the 50 m simulation being slightly smaller. In the two higher resolution simulations the thermocline has been raised above its rest height behind the leading wave. This is indicated by the negative surface currents. This feature is missing in the 100 m resolution simulation for which the surface currents remain positive between the two leading solitary waves and immediately behind the second solitary wave. At later times the 50 and 33 m resolution simulations diverge as well, becoming quite different at 85 m depth (Fig. 10d). The back

Shoaling internal solitary wavesK. G. Lamb and
A. Warn-Varnas

Title Page

Abstract

Introduction

Conclusions

References

Tables

Figures

◀

▶

◀

▶

Back

Close

Full Screen / Esc

Printer-friendly Version

Interactive Discussion



Shoaling internal solitary waves

K. G. Lamb and
A. Warn-Varnas

Title Page

Abstract

Introduction

Conclusions

References

Tables

Figures



Back

Close

Full Screen / Esc

Printer-friendly Version

Interactive Discussion



of the leading depression becomes very steep and is resolved by 4–5 grid points in the 50 m simulation. The jump is steeper in the 33 m resolution. Wave breaking has commenced behind the two leading depressions just before this time. The steep rear of the waves of depression and the commencement of overturning behind them is similar to that shown in Fig. 6 for bathymetry h_0 .

Also shown in Fig. 10d are results from a simulation with $\Delta x = 33$ m and double the vertical resolution ($J = 400$). These are indistinguishable from the case with half the vertical resolution. See also Fig. 13 below.

Similar tests were done using a larger wave (amplitude 115 m) using bathymetry h_0 . This wave is approximately half the width of the 45 m wave, requiring higher horizontal resolutions. The divergence between results for different resolutions was qualitatively similar to that in the above case however the divergence occurred more rapidly. Indeed, after travelling 8.5 km to a depth of 2800 there were already noticeable differences in wave amplitudes between the runs using $\Delta x = 250$, 100 and 33 m, with the wave in the 250 m resolution simulation already being over 5% smaller than that in the 33 m simulation, suggesting that at a depth of 3000 m the resolution needs to be significantly better than 250 m to accurately simulate waves of this amplitude.

While doubling the vertical resolution did not result in any significant changes in the leading waves it did reduce noise that developed in the deep water behind the waves. When a resolution of 200 grid points was used weak ($< 0.01 \text{ m s}^{-1}$) near surface currents (across the pycnocline at a depth of 50 m) developed over the steepest parts of the bathymetry, indicative of the pressure-gradient error that is intrinsic to sigma-coordinate models. With 400 grid points these currents were reduced by 50%. Simulations with a resolution of 300 and 400 vertical grid points were similar and were very expensive. Because the leading waves were unaffected by increasing the vertical resolution from 200 to 400 we have for the most part used a vertically varying grid with 200 grid points in the vertical. The grid has almost uniformly spaced grid cells for depths greater than 700 m and less than 300 m in deep and shallow water with a transition region centred at 500 m depth. In deep water the resolution was between 21.1 and

21.4 m at depths greater than 700 m and decreases from 6 m in depths at 350 m depth to 5.35 m at the surface. The vertically varying grid better resolves the thermocline in deep water. In water with depths less than 350 m the resolution is almost uniform, with $dz = 0.4$ m on the shelf. This grid gave virtually identical results to the vertically uniform grid using 400 vertical grid points.

3.2 Adiabaticity of shoaling waves

Solitary waves are said to shoal adiabatically if they retain the form of a single solitary wave as they shoal, i.e. no fissioning or reflection occurs (Grimshaw et al., 2004; Vlasenko et al., 2005). This can only occur if the water depth changes sufficiently slowly so that the shoaling wave can adapt to its new depth. Adiabatically shoaling waves conserve energy to leading-order in amplitude (in the absence of rotational effects) however they are in general trailed by a long small amplitude shelf which extends from the back of the solitary wave to the point reached by a wave travelling at the long wave propagation speed generated at the point when the shoaling solitary wave first encounters a depth change (Grimshaw et al., 2004). Because energy is second-order in amplitude the energy in the trailing shelf is negligible, however the mass in the shelf, being first-order in amplitude, can be significant.

In this section we investigate the adiabaticity of the shoaling waves by comparing the leading wave to ISW solutions of the DJL equation having the same total energy as the initial deep water wave. Both bathymetries h_0 and h_{15} are used. In addition we compare the shoaling behaviour of waves starting in different water depths using bathymetry h_0 . For these comparisons the bathymetries differ only in that they level off at three different deep water depths, namely 3000, 1500 and 1000 m as illustrated in Fig. 11. The base stratification was used except where noted.

Internal wave solutions of the DJL solution were computed over a range of water depths for 11 values of the APE: 25 MJ m^{-1} and 50 to 500 MJ m^{-1} in increments of 50 MJ m^{-1} . Figure 12a shows the total wave energy E (KE plus APE) as a function of depth for these 11 values. In Fig. 12b the ratio of kinetic to available potential energy

Shoaling internal solitary waves

K. G. Lamb and
A. Warn-Varnas

Title Page

Abstract

Introduction

Conclusions

References

Tables

Figures



Back

Close

Full Screen / Esc

Printer-friendly Version

Interactive Discussion



Shoaling internal solitary waves

K. G. Lamb and
A. Warn-Varnas

Title Page

Abstract

Introduction

Conclusions

References

Tables

Figures



Back

Close

Full Screen / Esc

Printer-friendly Version

Interactive Discussion



is shown. This ratio is always greater than one for solitary waves (Lamb and Nguyen, 2009). In the deep water (depth 3000 m) this ratio varies from slightly more than 1 to a maximum of 1.2 for the largest wave (amplitude 137 m) for which values are plotted. For larger waves (not shown) this ratio continues to increase, reaching 1.3 for an APE of 800 MJ m⁻¹ and 1.4 for an APE of 2 GJ m⁻¹. The 800 MJ m⁻¹ wave has an amplitude of 170 m and a minimum Richardson number of just below 0.25 in the thermocline. The 2 GJ m⁻¹ wave has an amplitude of 322 m, a minimum Richardson number of 0.11 and the ratio of the maximum current to the propagation speed is $\max(u)/c = 0.98$. Waves with $\max(u)/c > 1$ have cores of recirculating fluid. As the water depth decreases from 3000 m with the APE fixed the total wave energy increases, reaching a peak value at depths between about 400 and 1200 m for small and large waves ($KE/APE \approx 1.16$ and 1.3 respectively, see Fig. 12b). As the depth decreases further the total energy rapidly decreases to twice the APE. This near equipartition of energy suggests waves of smaller amplitude. This is indeed borne out in Fig. 13 which shows the wave amplitude (maximum isopycnal displacement), maximum surface current and maximum bottom current (negative for rightward propagating waves of depression) as a function of depth for constant total energies E of 50 MJ m⁻¹ and 100 to 1000 MJ m⁻¹ in increments of 100 MJ m⁻¹. These values were obtained by interpolating results from the DJL solutions, for which the APE is prescribed, and will be referred to as the adiabatic curves: these are the curves a shoaling wave would follow if the wave preserved its total energy and had the form of a solitary wave at each depth. As the water depth decreases from 3000 m the wave amplitude increases significantly, reaching a maximum value in depths between 300 and 600 m. The largest wave (total energy of 1 GJ m⁻¹) increases in amplitude by a factor of 1.4 from 129 to 183 m. For smaller waves the amplitudes increase by larger factors as the depth decreases (e.g. 3.5, 2.9 and 2.3 for the three smallest waves). Once shallow water is reached the amplitudes decrease rapidly and all waves have an amplitude close to 60 m in water of 200 m depth. This is an indication of the conjugate flow limit being attained: the waves all have the same

maximum amplitude and as the wave energy increases the waves get longer with negligible increases in amplitude.

The adiabatic curves are similar for the other two stratifications. Table 2 gives the initial and maximum amplitudes and the depth at which the maximum amplitude occurs for ISW solutions of the DJL equation for waves of fixed total energy. The maximum amplitudes and depths are based on values computed at depth intervals of 50 m. Values for all three stratifications are provided. The increase in amplitude of the waves is similar for stratifications $\bar{\rho}_b$ and $\bar{\rho}_1$ while waves using stratification $\bar{\rho}_2$ show a larger amplitude increase, particularly for small waves.

A similar pattern is seen for the maximum surface currents except that the maximum currents occur in greater depths than do the maximum wave amplitudes and the range of depths at which near-maximum currents occur is much wider than those for near-maximum amplitudes. The bottom currents reach their maximum values in much shallower water and the increase over their deep water values is much larger than the increases in wave amplitude and surface currents.

Figure 13 also shows the maximum wave amplitude, maximum surface current and minimum currents at the bottom from several simulations. Results using bathymetry h_0 (including the modified bathymetries leveling off at depths of 1500 and 1000 m) are shown in blue while results using bathymetry h_{15} are shown in red. For these simulations the Coriolis parameter was set to zero, as the adiabatic curves are only appropriate in the absence of rotation. Five simulations were done using bathymetry h_0 for waves starting in a depth of 3000 m. Four of these used a horizontal resolution of about 33 m with 200 uniformly spaced grid points in the vertical. These waves had APEs of 50, 100, 250 and 400 MJ m⁻¹ and are shown with solid blue curves. The fifth case (green dots), also with an APE of 400 MJ m⁻¹, used double the vertical resolution. It largely overlies the corresponding lower resolution case, although it has slightly larger amplitudes in depths between 600 and 800 m. Results from four simulations starting at 3000 m depth using bathymetry h_{15} are also shown (red curves). The initial APEs for these waves were 100, 150, 250 and 400 MJ m⁻¹. Results from simulations starting

Shoaling internal solitary waves

K. G. Lamb and
A. Warn-Varnas

[Title Page](#)[Abstract](#)[Introduction](#)[Conclusions](#)[References](#)[Tables](#)[Figures](#)[Back](#)[Close](#)[Full Screen / Esc](#)[Printer-friendly Version](#)[Interactive Discussion](#)

Shoaling internal solitary waves

K. G. Lamb and
A. Warn-Varnas

Title Page

Abstract

Introduction

Conclusions

References

Tables

Figures



Back

Close

Full Screen / Esc

Printer-friendly Version

Interactive Discussion



point the amplitude and maximum surface current of the wave with an initial APE of 100 MJ m^{-1} ($E = 204 \text{ MJ m}^{-1}$) is well below those for the DJL waves with an initial APE of 50 MJ m^{-1} . After this the amplitudes and surface currents rise rapidly and fall tracking the adiabatic curves in depths less than about 700 m. This suggests significantly non-adiabatic shoaling over the steep slope and nearly adiabatic shoaling over the gentle slope between depths of 750 and 80 m. Similar behaviour is observed for the waves launched from a depth of 1000 m. Of these waves, in depths less than about 700 m the wave with an initial APE of 60 MJ m^{-1} has nearly identical amplitude and maximum surface currents to that of the wave with an initial APE of 100 MJ m^{-1} launched from a depth of 3000 m.

Results obtained using bathymetry h_{15} show a similar pattern. Because this bathymetry is much steeper than h_0 for depths between 500 and 2300 m, the results with this bathymetry (red curves) do not follow the adiabatic curves until the waves reach much shallower depths of between 500 and 600 m. The effects of the bump at a depth of 600 m are clearly visible. The large loops in the wave amplitudes, particularly evident in the smaller waves, are a consequence of the largest vertically displacements occurring behind the bump after the solitary wave passes over it, rather than in the solitary wave itself, for a short period of time.

In water shallower than about 400 m the large shoaling waves have amplitudes that exceed the conjugate flow limit: at 350 and 200 m depths the largest shoaling waves have amplitudes of 142 and 95 m while the corresponding conjugate flow amplitudes are 137 and 61 m. Surface currents do not exceed the conjugate flow limits until depths of 250 m are reached. This increase in surface currents is associated with the very steep backs of the waves which are close to overturning for large waves (e.g. see Fig. 17f below).

Figure 13c shows the evolution of the largest amplitude bottom currents. The most striking feature of these results is that the bottom currents greatly exceed those for the DJL solutions in water shallower than about 300 m for the large waves and about 200 m for the smaller waves. This is a consequence of the fluid below the thermocline

being squeezed out from beneath the waves as the waves shoal which, in shallow water, results in enhanced bottom currents. This has important implications for the occurrence of instabilities, mixing and sediment resuspension beneath the shoaling wave. Also noteworthy is that for the large waves the bottom current increases relative to the adiabatic curves as the waves shoal to about 500 m depth. For the smaller waves they decrease as do the amplitudes and surface currents. For large waves in shallow water the bottom currents greatly exceed the surface currents.

3.3 Sensitivity to initial water depth

Figure 14 compares the horizontal currents at the surface for the waves with initial APEs of 60 and 100 MJ m⁻¹ launched from depths of 1000 and 3000 m respectively using bathymetry h_0 . The latter case is the same one illustrated in Fig. 5. Figure 15 shows the corresponding $\sigma_t = 0.0232$ isopycnal at the same times. This isopycnal was chosen because it is at the depth of maximum buoyancy frequency in the undisturbed stratification. It is not the isopycnal which undergoes maximum vertical displacement in the wave. The latter isopycnal varies with wave amplitude and varies as the wave shoals.

These two waves are chosen because in shallow water the leading waves have nearly identical amplitude. At a depth of 750 m the wave launched from a depth of 1000 m is about 15 km past the bottom of its shelf slope while the wave started from deeper water is about 150 km beyond the bottom of its shelf slope. Both waves are asymmetric, with the wave launched from deeper water being much more asymmetric. Recall that at a depth of 750 m the shelf slope decreases from 0.03 to 0.004. By the time the wave have reached a depth of 560 m (Fig. 14b) the initial wave has fissioned into multiple waves. The wave launched from the deeper water has fissioned into three solitary waves at $x = -40, -45$ and -49 km (the third is just starting to emerge) while the wave launched from the shallower depth has fissioned into two (at $x = -40$ and -46 km). The leading waves are very similar in amplitude (by choice). By the time the leading waves have reached a depth of 250 m (Fig. 14c) the multiple solitary waves

Shoaling internal solitary waves

K. G. Lamb and
A. Warn-Varnas

Title Page

Abstract

Introduction

Conclusions

References

Tables

Figures



Back

Close

Full Screen / Esc

Printer-friendly Version

Interactive Discussion



Shoaling internal solitary wavesK. G. Lamb and
A. Warn-Varnas

Title Page	
Abstract	Introduction
Conclusions	References
Tables	Figures
◀	▶
◀	▶
Back	Close
Full Screen / Esc	
Printer-friendly Version	
Interactive Discussion	



produced via fissioning are well separated. In the case of the wave launched in deep water the second wave trails the first by about 9 km and the third wave is a further 6 km behind. The third wave has a similar amplitude and location to that of the second wave for the case started at 1000 m depth. By the time the waves have reached depths of about 120 m (Fig. 14d) the leading wave has deformed considerably. The wave has broadened considerably. Steep front and backs (at about $x = 69$ and 66 km) are separated by a region in which u varies slowly and the isopycnals (see Fig. 5d) are close to parallel with the bottom. Behind the leading wave u is now strongly negative with currents almost equal in magnitude to the positive currents in the leading wave of depression. This is indicative of a large wave shelf trailing the leading wave of depression. The trailing waves have advanced relative to the leading wave as they are in deeper water and have larger propagation speeds. The third wave in the deep water case has now split into two waves.

As the waves pass the critical point and reach their final depth of 80 m (Fig. 14e and f) the leading wave continues to broaden and the currents decay in amplitude. The second wave in the deep water case advances into the wave shelf trailing the leading wave (the region of negative surface current) with the result that the wave forms behind the leading depression are quite different for the two cases.

3.4 Effects of bumps

The deep bump on bathymetry h_0 does not significantly affect the evolution of the shoaling waves. The much shallower bump on bathymetry h_{15} has a significant impact. Figure 16 compares the wave fields at $t = 29$ h for simulations with and without the bump at 700 m depth for an initial wave amplitude of 59 m. For the bathymetry with the bump the leading three waves are at $x = 41.0, 35.9$ and 31.8 km. With the bump removed the waves are slightly ahead, at $x = 42.8, 37.3$ and 33.7 km which we attribute to the reduction in propagation speed as the wave passes over the bump. The leading three waves are similar in amplitude when compared at times chosen so that these waves are at the same location with the waves in the no-bump case being slightly

larger. This is illustrated in Fig. 16b and d which show the two wave fields at slightly different times, chosen so the leading waves are at approximately the same location. The most striking difference between the two simulations is the wave field behind the leading three waves. For bathymetry h_{15} a mode-one wave train trails the leading three waves. Following are higher mode waves, e.g. at time $t = 29$ (Fig. 16a), a mode-two wave between $x = 0$ and 6 km can be seen with higher mode waves further behind. At the later times mode-two waves in both simulations are clearly apparent but are much larger in the simulation with the bump (e.g. $t x = 18$ and 30 km for the case with a bump, and at $x = 20$ km in the case with no bump).

3.5 Sensitivity to initial wave amplitude

Figure 17 compares the shoaling behaviour for three initial waves (amplitudes 45, 83 and 115 m) using the base stratification $\bar{\rho}_b$ and bathymetry h_{15} (Cases 3, 6, and 7). Times for comparison are chosen so that the leading waves are in approximately the same location. For the smallest initial wave there are two large solitary waves at $t = 35$ h (Fig. 17b) whereas for the two larger waves there are three. The intermediate wave has a number of smaller solitary waves trailing the leading large waves that are absent in the two cases with smaller and larger initial waves. Another noticeable feature is that for the largest wave, the leading wave is proportionally much larger than the trailing waves (see Fig. 17f) than in the other two cases.

3.6 Effects of rotation

The effects of rotation on the evolution of the internal tide and on ISWs has been considered by many authors (e.g. Helfrich, 2007; Helfrich and Grimshaw, 2008). Rotation makes long wave dispersive and as a consequence ISWs radiate long inertia-gravity (Poincaré) waves behind them and gradually decrease in amplitude. In some regions of parameter space the long radiated waves steepen and form new ISW packets (Helfrich, 2007). This process takes place on the inertial time period which in the South China

Shoaling internal solitary waves

K. G. Lamb and
A. Warn-Varnas

Title Page

Abstract

Introduction

Conclusions

References

Tables

Figures



Back

Close

Full Screen / Esc

Printer-friendly Version

Interactive Discussion



(between $x = 10$ and 20 km). These waves are larger in the rotating case which could be a consequence of the presence of the radiated Poincaré wave.

In Fig. 19 we plot the amplitude of the leading wave as a function of x as the waves shoal. Results for five pairs of simulations (with and without rotation) using different initial wave amplitudes are shown (cases 3–7). In the absence of rotational effects the waves slowly increase in amplitude until the bump ($x = -20$ km) is reached. At this stage the wave fissions and the amplitudes of the three smallest waves momentarily decrease. All waves then rapidly increase in amplitude. The largest wave reaches its peak amplitude just before the crest of the bump is reached, then maintains its amplitude before starting to decrease in amplitude rapidly at $x = 40$ km (420 m depth). The other waves reach their maximum amplitude between $x = 40$ and 50 km (depths of 400–300 m) before rapidly decreasing until the shelf is reached at $x = 80$ km with smaller waves reaching their maximum amplitude in shallower water.

When rotational effects are included the wave amplitude immediately starts to decrease, approximately linearly with x . After passing over the bump at $x = -20$ km the effects of rotation no longer seem to be prominent. For example, consider case with an initial amplitude of 59 m ($APE = 150 \text{ MJ m}^{-1}$). By $x = -20$ km its amplitude is close to that of the smaller wave in the non-rotating case. As the waves continue to shoal they remain similar in amplitude although the waves in the rotating case do continue to reduce relative to those in the non-rotating cases. In all cases the waves increase significantly in amplitude after reaching depths of about 800 m. At 200 m depth ($x = 60.7$ km) all waves significantly exceed the 60 m conjugate flow amplitude limit except for the smallest wave with rotational effects.

3.7 Sensitivity to stratification

Figure 20 compares waves fields for two case using bathymetry h_{15} , $f = 0$ and an initial wave APE of 50 MJ m^{-1} . Figure 20a, c, e and b, d, f shows results using density profiles $\bar{\rho}_1$ and $\bar{\rho}_2$ respectively. Consider stratification $\bar{\rho}_1$. Figure 20a shows the leading waves at $t = 36$ h at which point there are two solitary-like waves at $x = 63$ and 65 km. They

Shoaling internal solitary waves

K. G. Lamb and
A. Warn-Varnas

Title Page

Abstract

Introduction

Conclusions

References

Tables

Figures



Back

Close

Full Screen / Esc

Printer-friendly Version

Interactive Discussion



Shoaling internal solitary waves

K. G. Lamb and
A. Warn-Varnas

Title Page

Abstract

Introduction

Conclusions

References

Tables

Figures



Back

Close

Full Screen / Esc

Printer-friendly Version

Interactive Discussion



are deforming due to the presence of the bottom showing the typical profile of a steep rear and more gently sloping front. Trailing is a long small amplitude mode-one wave of elevation centred at about $x = 47$ km. This long mode-one wave, being in deeper water, is propagating faster than the leading wave packet and eventually catches up to it (not shown) with little effect because of its small amplitude. Trailing the mode-one waves are mode-two waves. The leading large mode-two wave can be seen at $x = 47$ – 53 km at $t = 47$ h (Fig. 20c). The mode-two wave is steepening and by $t = 55$ h has evolved into a packet of four mode-two waves with the leading front at $x = 67$ km (Fig. 20e). The wave crests are separated by about 750 m. Trailing the packet of short mode-two waves is a long mode-two concave wave ($x \approx 58$ km) and a long convex mode-two wave ($x \approx 45$ km). Both convex and concave mode-two internal waves have been observed on the Chinese continental slope in the South China Sea (Yang et al., 2010).

Figure 20b, d and f shows results from a similar case using stratification $\bar{\rho}_2$. Figure 20b shows the wave field at $t = 38$ h 20 min. This time was chosen so that the leading wave is at the same location as for the case using $\bar{\rho}_1$. In this case there are three solitary-like waves. A long mode-one wave centred at $x = 45$ km trails the leading wave packet. This wave is larger than the corresponding feature seen in Fig. 20a and by $t = 47$ h it has steepened to form a second mode-one wave packet seen at $x = 67$ km in Fig. 20d at which point a mode-two wave packet has just entered the region depicted in the figure. A long concave mode-two wave is present at $x = 53$ km. By $t = 55$ h this wave has sharpened and is more visible ($x = 65$ km in Fig. 20f), as is the trailing mode-two wave packet.

Figure 21 shows a similar comparison but for cases with rotational effects included. The leading wave packet now consists of a single solitary wave which is smaller than the leading wave in the non-rotating cases. At $t = 43$ h for the case with $\bar{\rho}_1$ a mode-one solitary wave packet can be seen at $x = 67$ km. This feature is not present in the non-rotating case. It has evolved from the evolution of the mode-one wave that can be seen at $x = 42$ km in Fig. 21a. For $\bar{\rho}_2$ (Fig. 21d) the mode-one wave packet at $x = 57$ km corresponds to the wave packet seen in the non-rotating case (Fig. 20d). The waves

have much larger amplitude in the rotating case. The mode-two wave seen Fig. 21e and f are similar to those seen in the non-rotating case.

3.8 Effects of viscosity and boundary layer separation

Some simulations were done with vertical eddy viscosity/diffusivity. A vertically varying viscosity/diffusivity of the form

$$\nu = \kappa = Kf(z) = K \operatorname{sech} \left(\frac{z - h(x)}{h_s} \right) \quad (3)$$

was used with a scale height $h_s = 10.0$ m. The dimensionless function $f(z)$ is shown in Fig. 22. The diffusivity/viscosity has a maximum value of K at the bottom and decreases by factors of 10 and 100 approximately 30 and 53 m above the bottom. This form of the viscosity/diffusivity coupled with a no-slip bottom boundary condition results in flow separation and vortex shedding at the back of the shoaling ISWs (Lamb and Nguyen, 2009; Boegman and Ivey, 2009; Lamb, 2014).

Figure 23 compares results from an inviscid simulation (Fig. 23a and b) with results from simulations with $K = 10^{-5}$, 10^{-4} and $10^{-3} \text{ m}^2 \text{ s}^{-1}$. At the stage illustrated, the four solutions have just become noticeably different (when the lead waves are at $x = 59$ km all four results are very similar). For $K = 10^{-5} \text{ m}^2 \text{ s}^{-1}$ the most noticeable difference is the enhancement of the positive near bottom currents behind the leading wave of depression ($x = 68.5$ km). This is consistent with flow separation and the formation of a vortex behind the leading depression as has been observed in the laboratory and in lab-scale numerical simulations. This positive current behind the leading depression is strengthened as K increases. For $K = 10^{-4} \text{ m}^2 \text{ s}^{-1}$ the waves are starting to deform. For the largest value of K the leading depression is significantly reduced in length and the trailing waves are smaller and show small scale features. In shallower water the differences between the four cases grow.

These results and results from other simulations not shown suggest that viscous effects are not significant until the waves reach depths less than about 200 m however in

Shoaling internal solitary waves

K. G. Lamb and
A. Warn-Varnas

Title Page

Abstract

Introduction

Conclusions

References

Tables

Figures



Back

Close

Full Screen / Esc

Printer-friendly Version

Interactive Discussion



Shoaling internal solitary wavesK. G. Lamb and
A. Warn-Varnas

Title Page	
Abstract	Introduction
Conclusions	References
Tables	Figures
◀	▶
◀	▶
Back	Close
Full Screen / Esc	
Printer-friendly Version	
Interactive Discussion	



deeper water the vertical resolution is reduced so these results are merely suggestive. In deep water the near bottom currents are much weaker which would reduce the affects of the bottom boundary layer beneath the shoaling waves. They also show that the presence of a turbulent bottom boundary layer beneath the waves could significantly affect shoaling solitary waves in water depths less than 200 m however these results are quite sensitive to the eddy viscosity. A more detailed investigation is needed.

4 Discussion and conclusions

Using a two-dimensional non-hydrostatic primitive equation model we have investigated aspects of the shoaling behaviour of internal solitary waves in the western South China Sea using bathymetry and stratifications based on observations made in the vicinity of the Asian Seas International Acoustic Experiment site (Orr and Mignerey, 2003; Duda et al., 2004; Ramp et al., 2004). Sensitivity to the stratification, the bathymetry and the effects of rotation were considered. The majority of the simulations were done without explicit viscosity. A few runs were done to explore the potential implications of a no-slip bottom boundary condition and the presence of a turbulent bottom boundary layer. Consideration of the effects of concurrent barotropic tides on shoaling ISWs are left for future work.

While waves with amplitudes close to 200 m have been observed in the deep part of the South China Sea (Klymak et al., 2006; Lien et al., 2012, 2014), we considered initial waves with amplitudes between 30 and 115 m in water 3000 m deep which are more typical (Li and Farmer, 2011). The adiabaticity of the shoaling was considered by tracking the wave amplitude and maximum wave induced currents as a function of water depth as the waves shoaled and comparing them with values for internal solitary waves with the same energy. We found some significant deviations from the adiabatic curves, with the amplitudes and currents during shoaling being significant less than those for an adiabatically shoaling wave. Thus the bathymetry in the vicinity of the ASI-AEX site is steep enough to result in significant deviations of the shoaling wave from

Shoaling internal solitary waves

K. G. Lamb and
A. Warn-Varnas

Title Page

Abstract

Introduction

Conclusions

References

Tables

Figures



Back

Close

Full Screen / Esc

Printer-friendly Version

Interactive Discussion



a solitary wave solution of the DJL equation with the same initial energy. Some energy is lost by fissioning of the initial wave into multiple waves. An example is that of Case 2 shown in Figs. 5 and 6. This case also illustrates the common occurrence of wave breaking in waves behind the leading depression (in this case at the back of the third wave of depression). Because of the very steep rear of the shoaling waves high horizontal resolutions were necessary. For most of our simulations we used a horizontal resolution of 33 m. The trailing waves did depend on the initial water depths. Comparisons of the shoaling behaviour of solitary waves with different deep water depths were done in which we tuned the amplitude of the wave starting in water of 1000 and 1500 m depths so that in water depths of less than 1000 m the leading waves had the same amplitude. The wave starting in the deeper water had larger trailing waves, an indication of the non-adiabatic nature of the shoaling even in deep water. Thus, in order to make detailed comparisons with observations it will be important to start at an appropriate deep water depth.

The bumps on the shelf slope topography influenced the shoaling behaviour, particularly the shallower bump on bathymetry h_{15} which is about 200 m high in water 700 m deep. As the shoaling wave passes over this bump higher mode waves are formed. As the bumps in the bathymetric transects are slices through three-dimensional features this implies that three-dimensionality of the bathymetry is likely an important factor in some locations, particularly for the secondary waves that form during shoaling.

In the absence of rotation, shoaling waves grow slightly in amplitude until they reach water depths of 800–1000 m after which they rapidly grow, reaching their maximum amplitude at depths between 250 and 600 m for initial amplitudes of 45 and 115 m respectively. They then decrease rapidly in amplitude but large waves can be 50% larger than the conjugate flow amplitude limit in water of 200 m depth. Rotation results in a continuous decrease in wave amplitude as waves shoal from 3000 m depth to 1000 m depth due to the continual radiation of inertia-gravity waves, but thereafter the waves undergo the same rapid rise and fall of their amplitude as the shoal into shallower water.

Shoaling internal solitary wavesK. G. Lamb and
A. Warn-Varnas

Title Page

Abstract

Introduction

Conclusions

References

Tables

Figures



Back

Close

Full Screen / Esc

Printer-friendly Version

Interactive Discussion



Ramp et al. (2004) presented time-depth temperature contour plots of internal waves at depths of 350, 200 and 120 m spanning an 11 day period. At 350 m depth they reported wave amplitudes (based on the 24° isotherm, hence amplitudes potentially underestimated) ranging between 29 and 142 m which matches well with the range of amplitudes in our simulations. Many features of the observed waves are similar to those seen in our simulations although there is naturally a great deal of variability in the observed waves. At 350 m depth waves both the observed and simulated waves were fairly symmetric. At 200 m depth many of the observed waves and all of the simulated waves were quite asymmetric (see also Fig. 4 in Orr and Mignerey, 2003 which shows acoustic images of an asymmetric wave close to this depth). As an example of a wave which is similar to one of our simulations consider the *a* wave observed at 08:00 GMT on 7 May (see Fig. 4 and Table III in Ramp et al., 2004). At 350 m depth it had an amplitude of 110 m and appears reasonably symmetric (note, however the difference in stratifications ahead and behind the wave suggesting that the observed wave is propagating at the front of a long depression). Four hours later it arrived at the 200 m depth mooring at which point it is quite asymmetric with the back of the wave being much steeper than the front of the wave. In our Case 6, which had an initial amplitude of 83.1 m, the leading wave had an amplitude of 117 m at 350 m depth at which point it was about 1.5 km in width and had a propagation speed of 1.6 m s⁻¹. Ramp et al. (2004) report a propagation speed of 1.33 m s⁻¹ and a width of 760 m (twice their reported half-width) for their observed wave. At 200 m depth the wave in our simulation had widened to 2 km and the propagation speed had decreased to 1.0 m s⁻¹. The wave was also asymmetric as is the observed wave (Ramp et al., 2004). Using a propagation speed of 1 m s⁻¹ the observed wave also has a width of about 2 km. By the time the observed waves have reached a depth of 120 they have broken up into many smaller waves including waves of elevation superimposed on broad depressions. Our simulations with viscosity suggest that by this depth the waves have been strongly modified by bottom boundary layer processes.

Shoaling internal solitary waves

K. G. Lamb and
A. Warn-Varnas

Title Page

Abstract

Introduction

Conclusions

References

Tables

Figures



Back

Close

Full Screen / Esc

Printer-friendly Version

Interactive Discussion



Our simulations also showed the formation of both convex and concave mode-two waves by the shoaling mode-one wave, as observed by Yang et al. (2009, 2010). These were more prominent for bathymetry h_{15} which had the shallow bump, and their presence and amplitude were sensitive to the stratification and to rotational effects.

An important process not considered in this study is the influence of barotropic tides and background currents on the shoaling of internal solitary waves. The advection of the shoaling wave by on-shelf and off-shelf tidal currents will decrease and increase the time the waves have to adjust – effectively increasing and decreasing the slope. In addition the on- and off-shelf motion will modify the stratification experienced by the waves and will generate other waves for the shoaling wave to interact with. Our simulations with near-bottom eddy viscosity suggest that the shoaling waves may be significantly modified by viscous effects in water shallower than 200 m, though our simulations are not well resolved in deep water so this remains an open question. Clearly much remains for us to learn about the evolution of shoaling ISWs.

Acknowledgements. This work is supported by the Office of Naval Research under PE 62435 (A. Warn-Varnas) and grants from the Natural Sciences and Engineering Research Council of Canada and the Canadian Foundation for Innovation (K. Lamb).

References

- Apel, J. R., Holbrook, J. R., Liu, A. K., and Tsai, J. J.: The Sulu Sea internal soliton experiment, *J. Phys. Oceanogr.*, 15, 1625–1641, 1985. 1165
- Boegman, L. and Ivey, G. N.: Flow separation and resuspension beneath shoaling nonlinear internal waves, *J. Geophys. Res.*, 114, c02018, doi:10.1029/2007JC004411, 2009. 1188
- Buijsman, M. C., Kanarska, Y., and McWilliams, J. C.: On the generation and evolution of nonlinear internal waves in the South China Sea, *J. Geophys. Res.*, 115, C10057, doi:10.1029/2009JC006004, 2010. 1165

Shoaling internal solitary waves

K. G. Lamb and
A. Warn-Varnas

Title Page

Abstract

Introduction

Conclusions

References

Tables

Figures

⏪

⏩

◀

▶

Back

Close

Full Screen / Esc

Printer-friendly Version

Interactive Discussion



- Duda, T. F., Lynch, J. F., Irish, J. D., Beardsley, R. C., Ramp, S. R., Chiu, C.-S., Tang, T. Y., and Y.-J. Yang: Internal tide and nonlinear wave behavior at the continental slope in the northern South China Sea, *IEEE J. Oceanic Eng.*, 29, 1105–1130, doi:10.1109/JOE.2004.836998, 2004. 1165, 1166, 1189
- 5 Farmer, D., Li, Q., and Park, J.-H.: Internal wave observations in the South China Sea: the role of rotation and non-linearity, *Atmos. Ocean.*, 47, 267–280, doi:10.3137/OC313.2009, 2009. 1164
- Grimshaw, R., Pelinovsky, E., and Poloukhina, O.: Higher-order Korteweg-de Vries models for internal solitary waves in a stratified shear flow with a free surface, *Nonlin. Processes Geophys.*, 9, 221–235, doi:10.5194/npg-9-221-2002, 2002. 1170
- 10 Grimshaw, R., Pelinovsky, E. N., Talipova, T. G., and Kurkin, A.: Simulations of the transformation of internal solitary waves on oceanic shelves, *J. Phys. Oceanogr.*, 34, 2774–2791, 2004. 1177
- Guo, C. and Chen, X.: A review of internal solitary wave dynamics in the northern South China Sea, *Prog. Oceanogr.*, 121, 7–23, doi:10.1016/j.pocean.2013.04.002, 2014. 1165
- 15 Helfrich, K. R.: Internal solitary wave breaking and run-up on a Uniform Slope, *J. Fluid Mech.*, 243, 133–154, 1992. 1166
- Helfrich, K. R.: Decay and return of internal solitary waves with rotation, *Phys. Fluids*, 19, 026601, doi:10.1063/1.2472509, 2007. 1184
- 20 Helfrich, K. R. and Grimshaw, R. H. J.: Nonlinear Disintegration of the Internal Tide, *J. Phys. Oceanogr.*, 38, 686–701, doi:10.1175/2007JPO3826.1, 2008. 1184
- Helfrich, K. R. and Melville, W. K.: On long nonlinear internal waves over slope-shelf topography, *J. Fluid Mech.*, 167, 285–308, 1986. 1166
- Hodges, B., Laval, B., and Wadzuk, B.: Numerical error assessment and a temporal horizon for internal waves in a hydrostatic model, *Ocean Model.*, 13, 44–64, doi:10.1016/j.ocemod.2005.09.005, 2006. 1174
- 25 Hsu, M.-K. and Liu, A. K.: Nonlinear internal waves in the South China Sea, *Can. J. Remote Sens.*, 26, 72–81, 2000. 1164
- Klymak, J. M., Pinkel, R., Liu, C.-T., Liu, A. K., and David, L.: Prototypical solitons in the South China Sea, *Geophys. Res. Lett.*, 33, L11607, doi:10.1029/2006GL025932, 2006. 1164, 1165, 1189
- 30 Lamb, K. G.: Numerical experiments of internal wave generation by strong tidal flow across a finite amplitude bank edge, *J. Geophys. Res.*, 99, 843–864, 1994. 1167

Shoaling internal solitary waves

K. G. Lamb and
A. Warn-Varnas

Title Page

Abstract

Introduction

Conclusions

References

Tables

Figures



Back

Close

Full Screen / Esc

Printer-friendly Version

Interactive Discussion



- Lamb, K. G.: A numerical investigation of solitary internal waves with trapped cores formed via shoaling, *J. Fluid Mech.*, 451, 109–144, 2002. 1169
- Lamb, K. G.: Energy and pseudoenergy flux in the internal wave field generated by tidal flow over topography, *Cont. Shelf Res.*, 27, 1208–1232, doi:10.1016/j.csr.2007.01.020, 2007. 1167
- Lamb, K. G.: Internal wave breaking and dissipation mechanisms on the continental slope/shelf, *Ann. Rev. Fluid Mech.*, 46, 231–254, doi:10.1146/annurev-fluid-011212-140701, 2014. 1188
- Lamb, K. G. and Nguyen, V. T.: Calculating energy flux in internal solitary waves with an application to reflectance, *J. Phys. Oceanogr.*, 39, 559–580, doi:10.1175/2008JPO3882.1, 2009. 1172, 1178, 1188
- Lamb, K. G. and Wan, B.: Conjugate flows and flat solitary waves for a continuously stratified fluid, *Phys. Fluids*, 10, 2061–2079, 1998. 1171
- Lamb, K. G. and Yan, L.: The evolution of internal wave undular bores: comparisons of a fully nonlinear numerical model with weakly nonlinear theory, *J. Phys. Oceanogr.*, 26, 2712–2734, 1996. 1170
- Li, Q. and Farmer, D. M.: The generation and evolution of nonlinear internal waves in the deep basin of the South China Sea, *J. Phys. Oceanogr.*, 41, 1345–1363, doi:10.1175/2011JPO4587.1, 2011. 1164, 1165, 1189
- Lien, R.-C., D'Asaro, E., Henyey, F., Chang, M. H., Tang, T. Y., and Yang, Y. J.: Trapped core formation within a shoaling nonlinear internal wave, *J. Phys. Oceanogr.*, 42, 511–525, doi:10.1175/2011JPO4578.1, 2012. 1189
- Lien, R.-C., Henyey, F., Ma, B., and Yang, Y. J.: Large-amplitude internal solitary waves observed in the northern South China Sea: properties and energetics, *J. Phys. Oceanogr.*, 44, 1095–1115, doi:10.1175/JPO-D-13-088.1, 2014. 1189
- Liu, A. K., Chang, Y. S., Hsu, M.-K., and Liang, N. K.: Evolution of nonlinear internal waves in the East and South China Seas, *J. Geophys. Res.*, 103, 7995–8008, 1998. 1164, 1166
- Lynch, J. F., Ramp, S. R., Chiu, C.-S., Tang, T. Y., Yang, Y.-J., and Simmen, J. A.: Research highlights from the Asian Seas International Acoustics Experiment in the South China Sea, *IEEE J. Oceanic Eng.*, 29, 1067–1074, doi:10.1109/JOE.2005.843162, 2004. 1165
- Niwa, Y. and Hibiya, T.: Numerical study of the spatial distribution of the M_2 internal tide in the Pacific Ocean, *J. Geophys. Res.*, 106, 22441–22449, 2001. 1165
- Niwa, Y. and Hibiya, T.: Three-dimensional numerical simulation of M_2 internal tides in the East China Sea, *J. Geophys. Res.*, 106, C04027, doi:10.1029/2003JC001923, 2004. 1165

Shoaling internal solitary waves

K. G. Lamb and
A. Warn-Varnas

Title Page

Abstract

Introduction

Conclusions

References

Tables

Figures

◀

▶

◀

▶

Back

Close

Full Screen / Esc

Printer-friendly Version

Interactive Discussion



- Orr, M. H. and Mignerey, P. C.: Nonlinear internal waves in the South China Sea: observation of the conversion of depression internal waves to elevation internal waves, *J. Geophys. Res.*, 108, 3064, doi:10.1029/2001JC001163, 2003. 1165, 1166, 1169, 1172, 1189, 1191
- Osborne, A. R. and Burch, T. L.: Internal solitons in the Andaman Sea, *Science*, 208, 451–460, 1980. 1165
- Ramp, S. R., Tang, T. Y., Duda, T. F., Lynch, J. F., Liu, A. K., Chiu, C.-S., Bahr, F. L., Kim, H.-R., and Yang, Y.-J.: Internal solitons in the northeastern South China Sea, Part I: Sources and deep water propagation, *IEEE J. Oceanic Eng.*, 29, 1157–1181, doi:10.1109/JOE.2004.840839, 2004. 1164, 1165, 1166, 1171, 1189, 1191
- Vitousek, S. and Fringer, O. B.: Physical vs. numerical dispersion in nonhydrostatic ocean modeling, *Ocean Model.*, 40, 72–86, doi:10.1016/j.ocemod.2011.07.002, 2011. 1174
- Vlasenko, V. and Hutter, K.: Numerical experiments on the breaking of solitary internal waves over a slope-shelf topography, *J. Phys. Oceanogr.*, 32, 1779–1793, 2002. 1166, 1172
- Vlasenko, V. and Stashchuk, N.: Three-dimensional shoaling of large-amplitude internal waves, *J. Geophys. Res.*, 112, C11018, doi:10.1029/2007JC004107, 2007. 1166
- Vlasenko, V., Ostrovsky, L., and Hutter, K.: Adiabatic behavior of strongly nonlinear internal solitary waves in slope-shelf areas, *J. Geophys. Res.*, 110, C04006, doi:10.1029/2004JC002705, 2005. 1177
- Vlasenko, V., Guo, C., and Stashchuk, N.: On the Mechanism of A-type and B-type internal solitary wave generation in the northern South China Sea, *Deep-Sea Res. Pt. I*, 69, 100–112, doi:10.1016/j.dsr.2012.07.004, 2012. 1165
- Warn-Varnas, A., Hawkins, J., Lamb, K. G., Piacsek, S., Chin-Bing, S., King, D., and Burgos, G.: Solitary wave generation dynamics at Luzon Strait, *Ocean Model.*, 31, 9–27, doi:10.1016/j.ocemod.2009.08.002, 2010. 1165, 1169, 1202
- Yang, Y. J., Fang, Y. C., Chang, M.-H., Ramp, S. R., Kao, C.-C., and Tang, T. Y.: Observations of Second Baroclinic Mode Internal Solitary Waves on the Continental Slope of the Northern South China Sea, *J. Geophys. Res.*, 114, C10003, doi:10.1029/2009JC005318, 2009. 1165, 1166, 1192
- Yang, Y. J., Fang, Y. C., Tang, T. Y., and Ramp, S. R.: Convex and concave types of second baroclinic mode internal solitary waves, *Nonlin. Processes Geophys.*, 17, 605–614, doi:10.5194/npg-17-605-2010, 2010. 1166, 1187, 1192

Zhao, X. and Alford, M. H.: Source and propagation of internal solitary waves in the northeastern South China Sea, J. Geophys. Res., 111, c11012, doi:10.1029/2006JC003644, 1989. 1164

Shoaling internal solitary waves

K. G. Lamb and
A. Warn-Varnas

Title Page

Abstract

Introduction

Conclusions

References

Tables

Figures



Back

Close

Full Screen / Esc

Printer-friendly Version

Interactive Discussion



Shoaling internal solitary waves

K. G. Lamb and
A. Warn-Varnas**Table 1.** Properties of Initial ISWs: 3000 m depth.

$\bar{\rho}$	\bar{E}_a (MJ m ⁻¹)	\bar{E}_k (MJ m ⁻¹)	a (m)	c (m s ⁻¹)	U_{\max} (m s ⁻¹)
$\bar{\rho}_b$	70.0	72.3	35.9	2.53	0.35
–	100.0	104.3	45.4	2.56	0.46
–	150.0	158.6	59.3	2.61	0.62
–	200.0	214.2	71.6	2.64	0.77
–	250.0	271.2	83.1	2.68	0.93
–	300.0	329.7	93.9	2.72	1.11
–	350.0	390.4	104.5	2.76	1.30
–	400.0	454.6	115.2	2.81	1.53
$\bar{\rho}_1$	50.0	51.0	26.29	2.57	0.23
–	100.0	103.2	41.72	2.60	0.38
–	150.0	156.6	54.70	2.64	0.53
$\bar{\rho}_2$	50.0	50.8	26.20	2.51	0.20
–	100.0	102.6	41.43	2.54	0.32
–	150.0	155.3	54.11	2.56	0.43

Title Page

Abstract

Introduction

Conclusions

References

Tables

Figures

◀

▶

◀

▶

Back

Close

Full Screen / Esc

Printer-friendly Version

Interactive Discussion



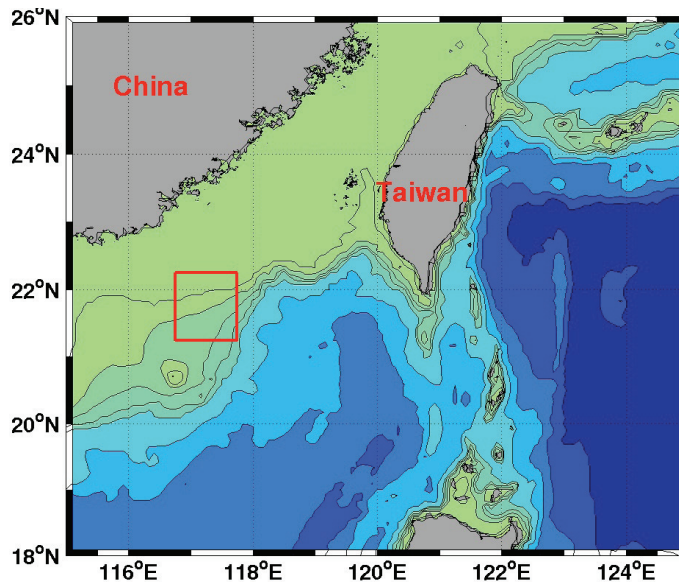
Shoaling internal solitary wavesK. G. Lamb and
A. Warn-Varnas

Figure 1. Luzon Strait and South China Sea region. Red square is location of ASIAEX experimental site.

[Title Page](#)[Abstract](#)[Introduction](#)[Conclusions](#)[References](#)[Tables](#)[Figures](#)[Back](#)[Close](#)[Full Screen / Esc](#)[Printer-friendly Version](#)[Interactive Discussion](#)

Shoaling internal solitary waves

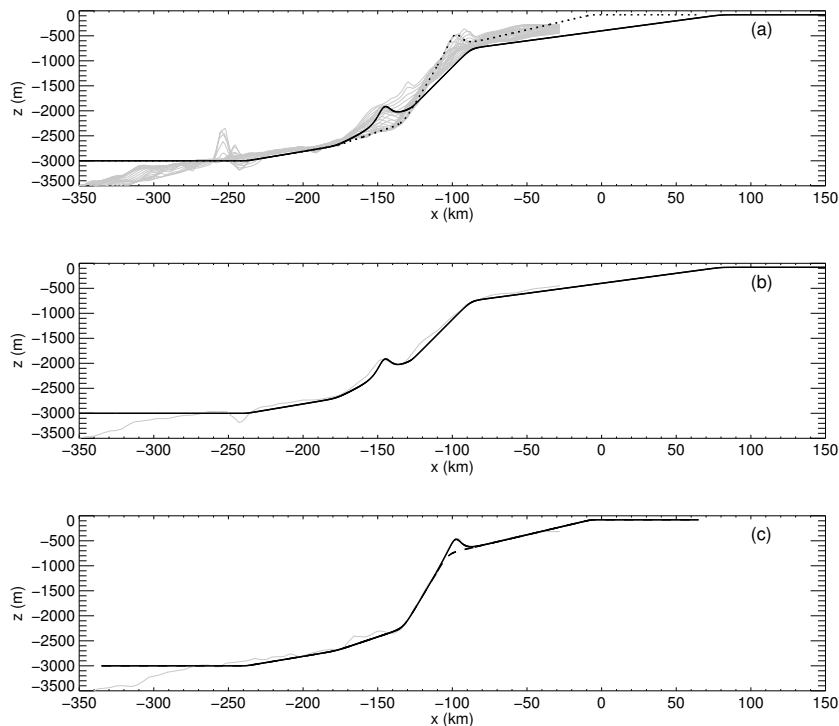
K. G. Lamb and
A. Warn-Varnas

Figure 2. Sample measured bathymetries at the ASIAEX location extracted from the Digital Bathymetry 2 min resolution (DB2) data base inside the red square area in Fig. 1. **(a)** Comparison of 24 different measured bathymetries (grey) with two model bathymetry (solid and dotted black curves). **(b)** Comparison of first model bathymetry, h_0 , (black) with one of the measured bathymetries (grey). **(c)** Comparison of two other model bathymetries (solid and dashed black curves) with a second measured bathymetry (grey). The solid curve is bathymetry h_{15} . The dashed curved is the same bathymetry with the bump at -100 km removed.

Title Page

Abstract

Introduction

Conclusions

References

Tables

Figures



Back

Close

Full Screen / Esc

Printer-friendly Version

Interactive Discussion



Shoaling internal solitary waves

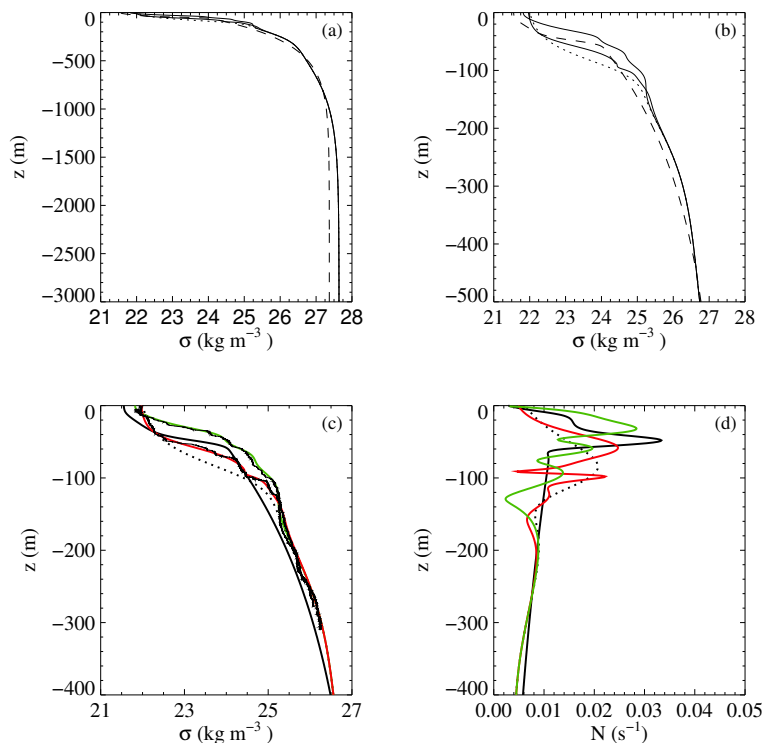
K. G. Lamb and
A. Warn-Varnas

Figure 3. Stratifications. **(a, b)** $\sigma = \rho - 1000 \text{ kg m}^{-3}$ for the base stratification (dashed) and two fits to observed stratifications (solid). Lower solid curve is $\bar{\rho}_1$. Upper solid curve is $\bar{\rho}_2$. For comparison the dotted line is the Luzon Strait stratification used in Warn-Varnas et al. (2010). **(c)** Stratifications in upper 400 m. Base stratification (thick black curve), $\bar{\rho}_1$ (red), $\bar{\rho}_2$ (green) and Luzon Strait stratification (dotted). Thin solid lines show corresponding observed density profile. **(d)** N (rad s⁻¹) for model stratifications shown in **(c)**.

Title Page

Abstract

Introduction

Conclusions

References

Tables

Figures

◀

▶

◀

▶

Back

Close

Full Screen / Esc

Printer-friendly Version

Interactive Discussion



Shoaling internal solitary waves

K. G. Lamb and
A. Warn-Varnas

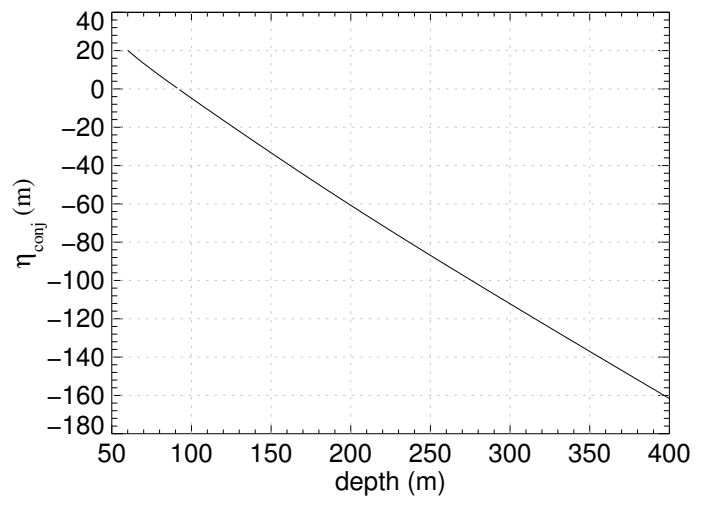


Figure 4. Conjugate flow amplitudes as a function of depth for stratification $\bar{\rho}_b$.

Title Page

Abstract

Introduction

Conclusions

References

Tables

Figures

◀

▶

◀

▶

Back

Close

Full Screen / Esc

Printer-friendly Version

Interactive Discussion



Shoaling internal solitary waves

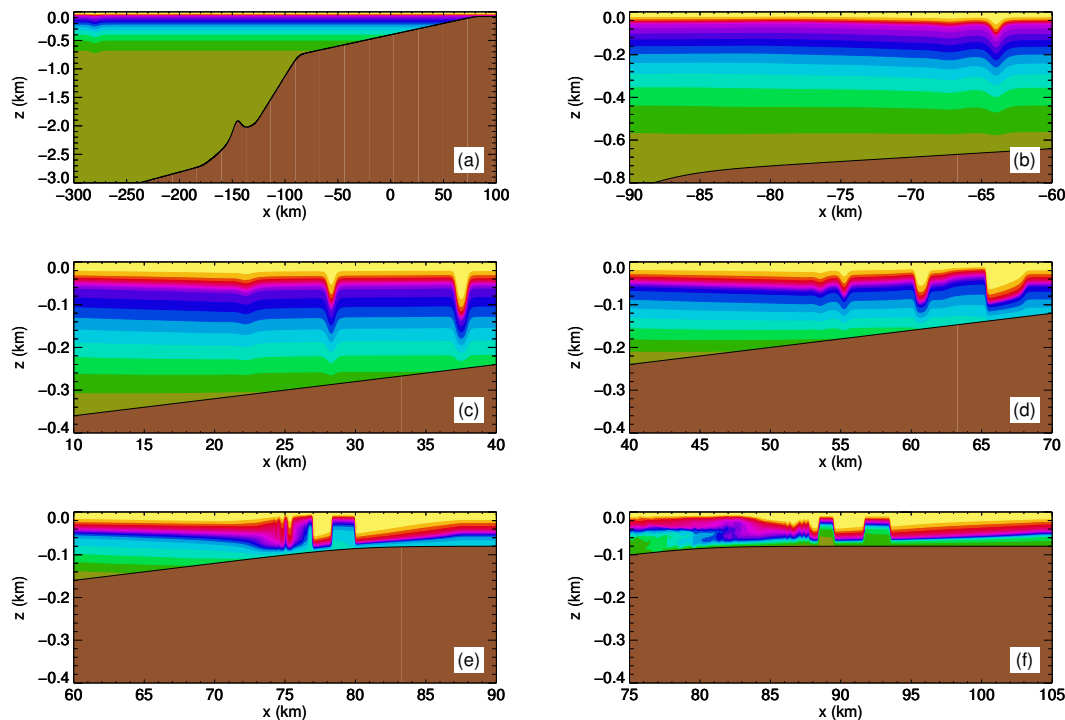
K. G. Lamb and
A. Warn-Varnas

Figure 5. Density fields for Case 2 using bathymetry h_0 . Resolution: $\Delta x = 33$ m, $J = 400$. Initial wave amplitude 45 m. **(a)** 0 h. **(b)** 25 h. **(c)** 42 h. **(d)** 50 h. **(e)** 58 h. **(f)** 66 h. The initial wave at $x = -280$ km is barely detectable at this scale.

Title Page

Abstract

Introduction

Conclusions

References

Tables

Figures

◀

▶

◀

▶

Back

Close

Full Screen / Esc

Printer-friendly Version

Interactive Discussion



Shoaling internal solitary waves

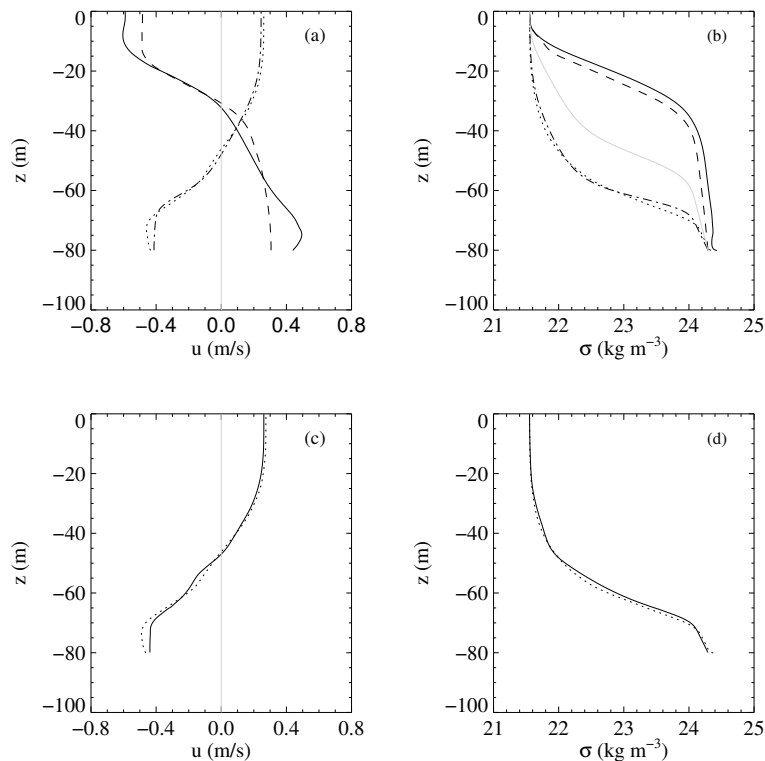
K. G. Lamb and
A. Warn-Varnas

Figure 7. (a, b) Vertical profiles of horizontal velocity and density for Case 2 at $t = 66$ h at locations shown in Fig. 6. **(a)** Horizontal velocity. **(b)** Density. Curves from second wave pedestal at $x = 89$ km (solid), the second depression at $x = 91$ km (dots), the first pedestal at $x = 92$ km (dashed), and in the leading depression at $x = 94$ km (dash-dot) (see Fig. 6 for profile locations). The light grey curve in **(b)** shows the background density profile. **(c, d)** Profiles in solitary waves of depression (solid) computed on background field given by profiles extracted from simulation in the pedestal at $x = 92$ km between the two leading waves of depression. Solution is compared with profiles taken from the second depression at $x = 91$ km (dots).

Title Page

Abstract

Introduction

Conclusions

References

Tables

Figures

◀

▶

◀

▶

Back

Close

Full Screen / Esc

Printer-friendly Version

Interactive Discussion



Shoaling internal solitary waves

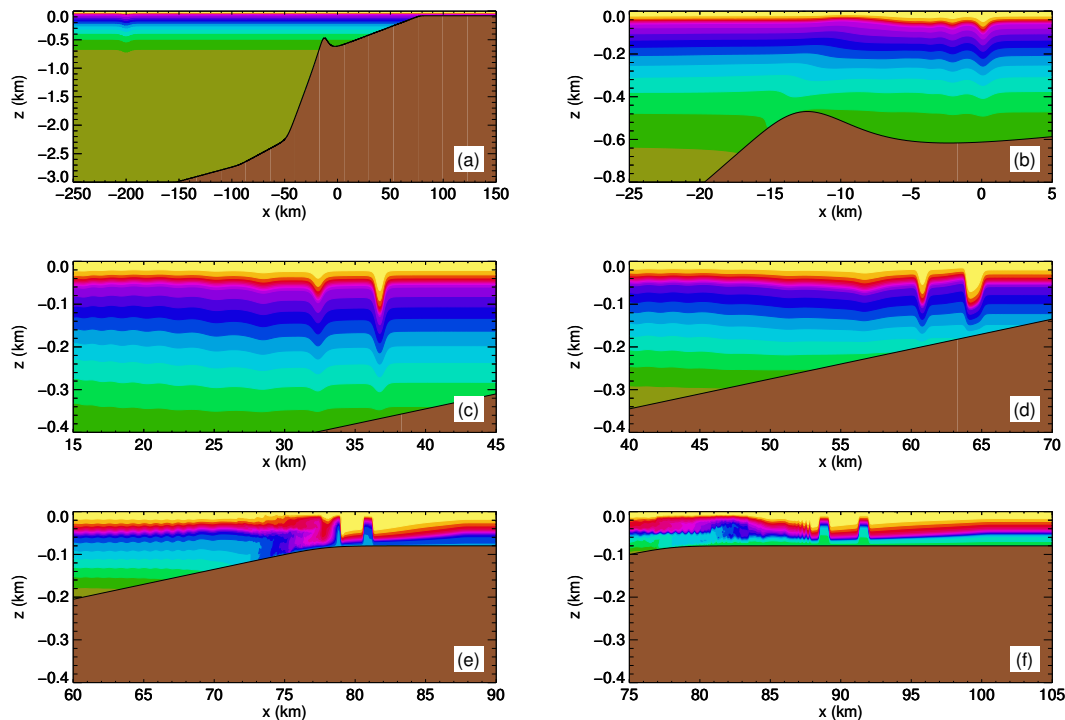
K. G. Lamb and
A. Warn-Varnas

Figure 8. Density fields for Case 3 using bathymetry h_{15} and stratification $\bar{\rho}_b$. Resolution: $\Delta x = 33$ m, $J = 400$. Initial wave amplitude 45 m, (APE = 100 MJ m^{-1}). **(a)** 0 h. **(b)** 23 h. **(c)** 29 h. **(d)** 35 h. **(e)** 44 h. **(f)** 50 h.

Title Page

Abstract

Introduction

Conclusions

References

Tables

Figures

◀

▶

◀

▶

Back

Close

Full Screen / Esc

Printer-friendly Version

Interactive Discussion



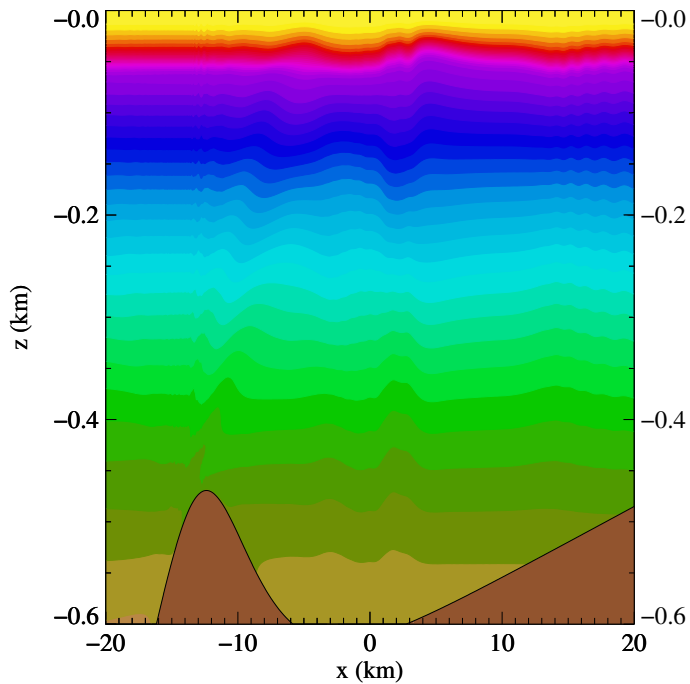


Figure 9. Density field for same case and time shown in Fig. 8c showing mode-two waves and an internal wave beam generated when the solitary wave passes over the bump.

Shoaling internal solitary waves

K. G. Lamb and
A. Warn-Varnas

Title Page	
Abstract	Introduction
Conclusions	References
Tables	Figures
◀	▶
◀	▶
Back	Close
Full Screen / Esc	
Printer-friendly Version	
Interactive Discussion	



Shoaling internal solitary waves

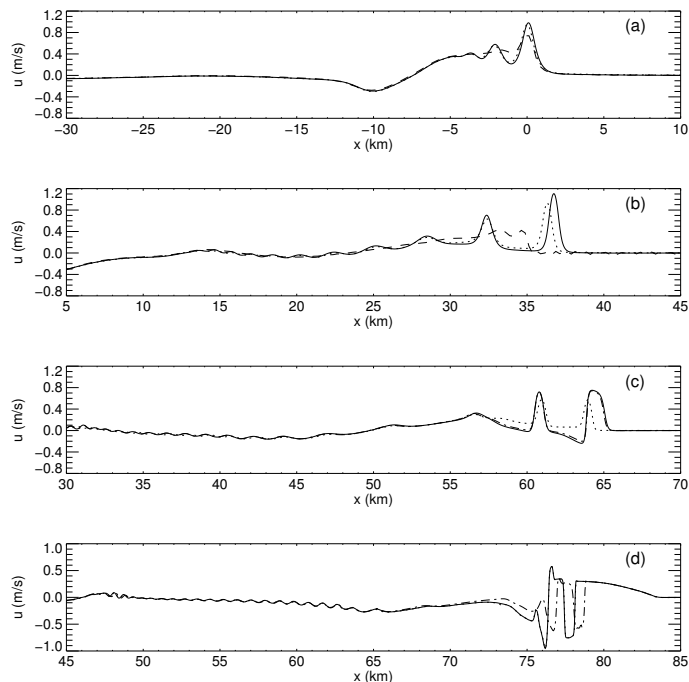
K. G. Lamb and
A. Warn-Varnas

Figure 10. Resolution tests. Shown are surface currents at four different depths for Case 3: bathymetry h_{15} and initial wave amplitude 45 m. Panels compare results from simulations with different horizontal resolutions using 200 grid points in the vertical: $\Delta x = 33$ m (solid), 50 m (dash-dot, **c**, **d** only), 100 m and 250 m (dashed, **a**, **b** only). **(a)** $t = 23$ h. Leading wave at 610 m depth – see Fig. 8b. **(b)** $t = 29$ h. Leading wave at 370 m depth – see Fig. 8c. **(c)** $t = 35$ h. Leading wave at 180 m depth – see Fig. 8d. **(d)** Results at $t = 42$ h. First depression in water shallower than 82 m. Second depression at 90 m depth. **(d)** Also includes results from simulation with $\Delta x = 33$ m and $J = 400$ points (dotted). This curve is indistinguishable from the solid curve.

Shoaling internal solitary waves

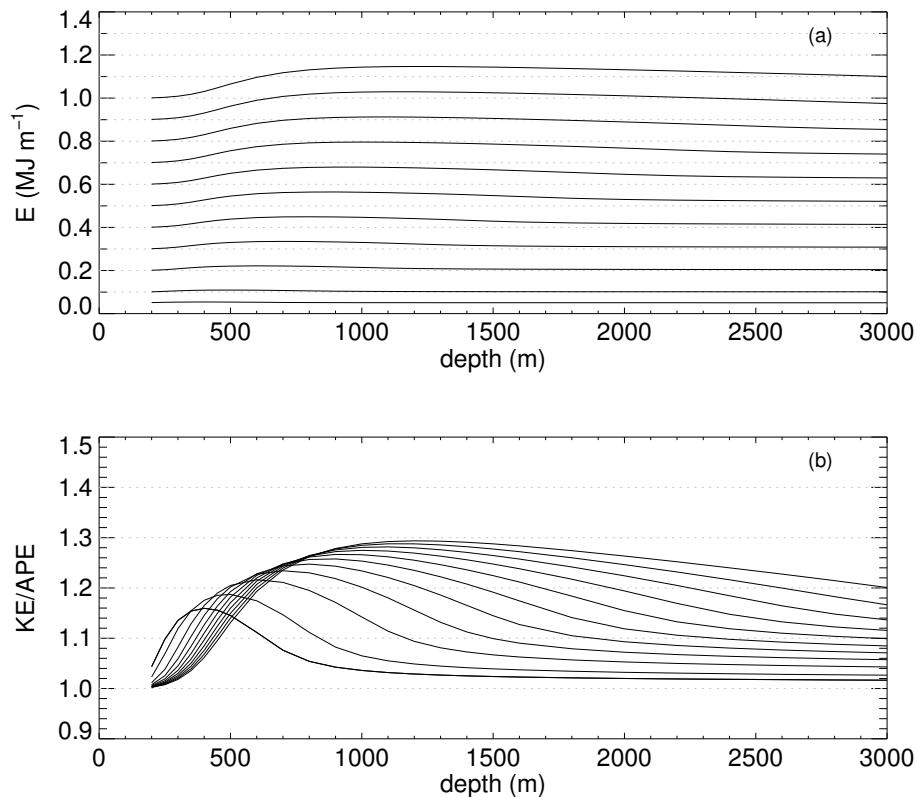
K. G. Lamb and
A. Warn-Varnas

Figure 12. (a) Total ISW energy (APE plus KE) for ISWs with fixed APE as a function of water depth. Curves are for APE equal to 25 MJ m^{-1} and 50 MJ m^{-1} to 500 MJ m^{-1} in increments of 50 MJ m^{-1} . (b) Ratio of KE to APE for same waves. On right side the ratio increases with APE.

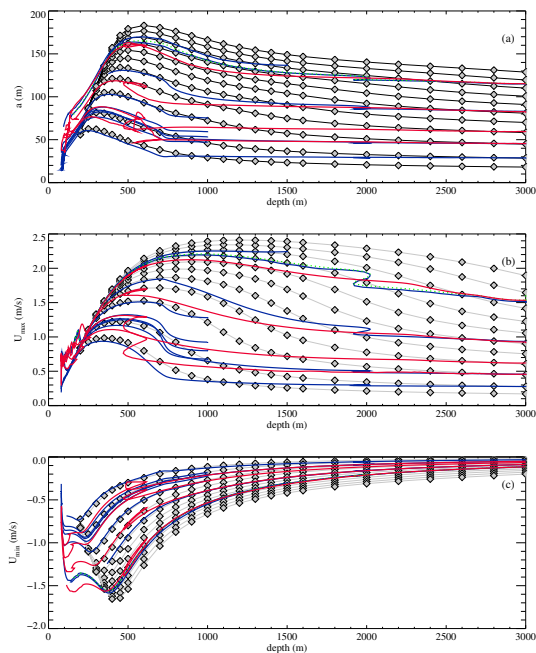


Figure 13. Wave properties as a function of water depth. **(a)** Wave amplitudes (absolute value), **(b)** maximum surface currents, **(c)** minimum bottom currents. Black curves with grey diamonds are for ISW solutions of the DJL equation for waves with total energy E equal to 50 MJ m^{-1} and 100 to 1000 MJ m^{-1} in increments of 100 MJ m^{-1} . Diamonds indicate computed values. Coloured curves are maximum absolute amplitude and surface current and minimum bottom currents of shoaling waves as function of water depth. Blue – cases using bathymetry h_0 . Red – cases using bathymetry h_{15} . Green-dotted – higher resolution case started at depth of 3000 m using bathymetry h_0 . This curve overlies the lower resolution result (blue curve, initial amplitude 115 m). Both are overlain by the results using bathymetry h_{15} for depths greater than about 2600 m .

Shoaling internal solitary waves

K. G. Lamb and
A. Warn-Varnas

Title Page

Abstract Introduction

Conclusions References

Tables Figures

◀ ▶

◀ ▶

Back Close

Full Screen / Esc

Printer-friendly Version

Interactive Discussion



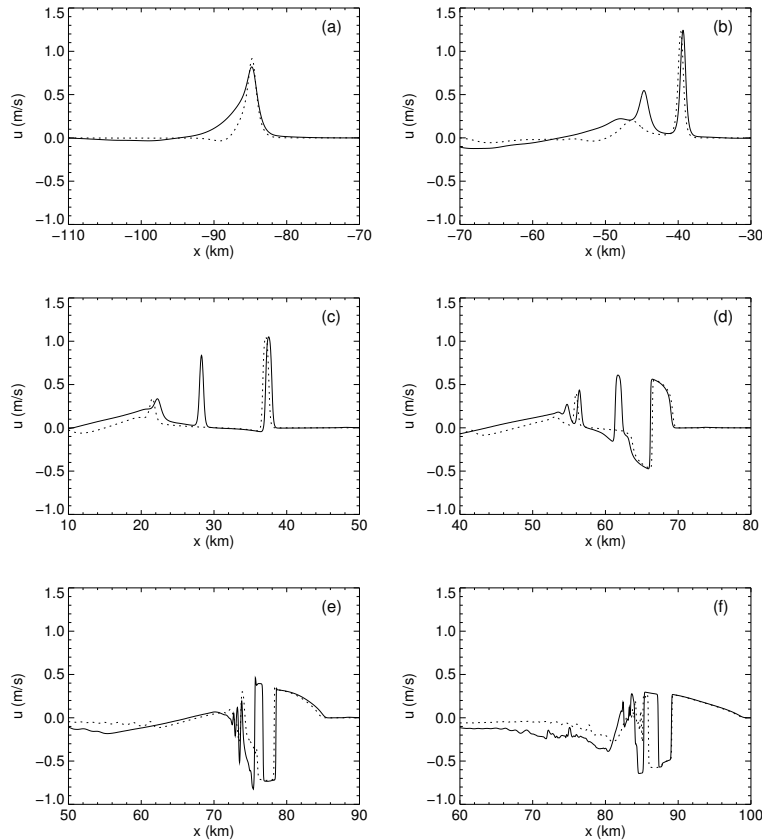


Figure 14. Horizontal velocity at the surface at different times for waves with initial APE of 100 and 60 MJ m^{-1} started at depths of 3000 (solid) and 1000 m (dashed) respectively using bathymetry h_0 . Times are different for the two waves, chosen so that the leading waves are at approximately the same location. Leading waves at depth of: **(a)** 750 m; **(b)** 560 m; **(c)** 250 m; **(d)** 135–120 m; **(e)** 90–80 m depth; and **(f)** 80 m.

Shoaling internal solitary waves

K. G. Lamb and
A. Warn-Varnas

Title Page	
Abstract	Introduction
Conclusions	References
Tables	Figures
◀	▶
◀	▶
Back	Close
Full Screen / Esc	
Printer-friendly Version	
Interactive Discussion	



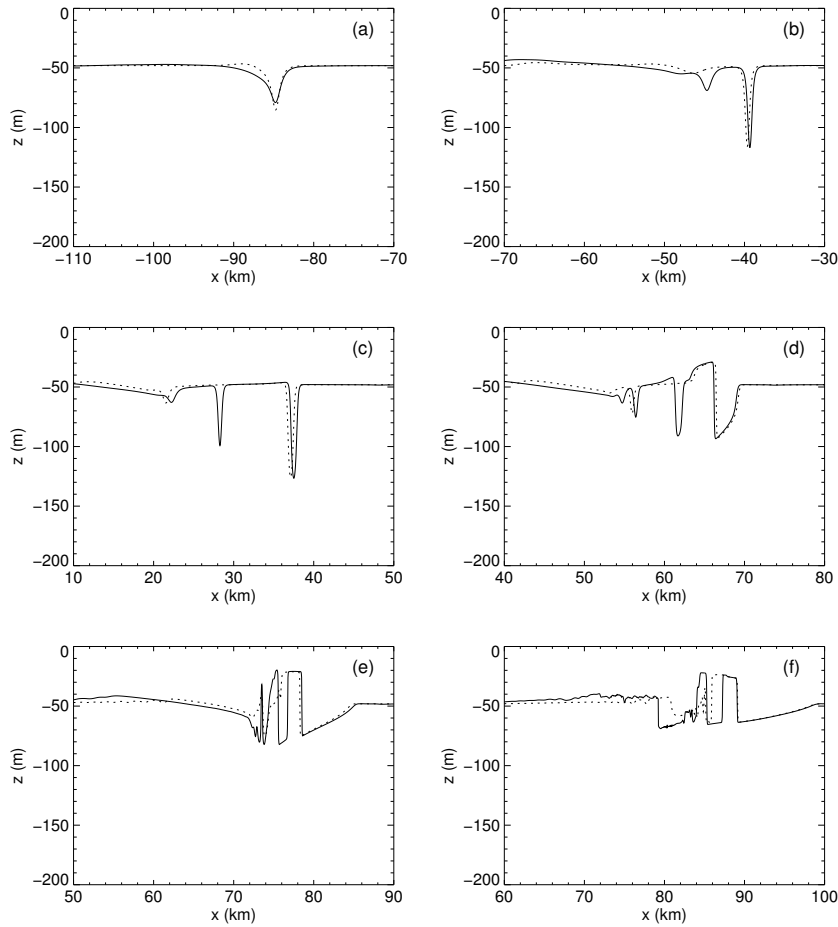


Figure 15. The $\sigma_t = 0.0232$ isopycnal. Same cases and times as in Fig. 14.

Shoaling internal solitary waves

K. G. Lamb and
A. Warn-Varnas

Title Page	
Abstract	Introduction
Conclusions	References
Tables	Figures
◀	▶
◀	▶
Back	Close
Full Screen / Esc	
Printer-friendly Version	
Interactive Discussion	



Shoaling internal solitary waves

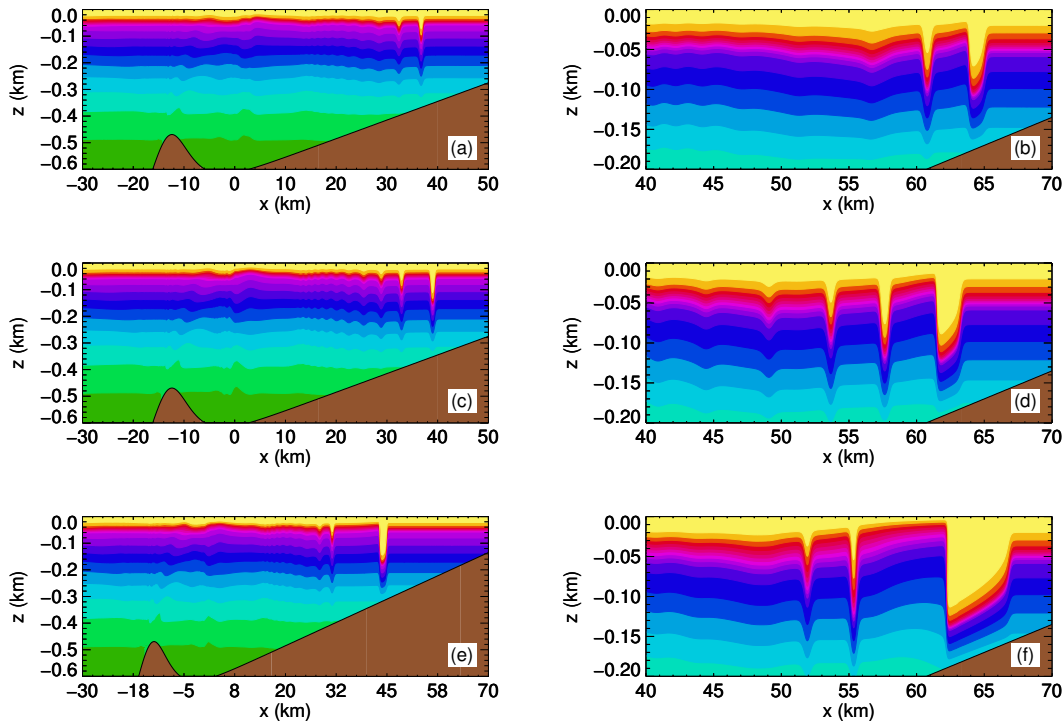
K. G. Lamb and
A. Warn-Varnas

Figure 17. Density fields for shoaling waves with different initial wave amplitudes using bathymetry h_{15} and stratification $\bar{\rho}_b$. **(a, b)** Case 3. Initial amplitude $a = 45$: results at $t = 29$ h and $t = 35$ h. **(c, d)** Case 6. Initial $a = 83$ m. Results at $t = 28$ and $t = 34$ h. **(e, f)** Case 7. Initial amplitude $a = 115$ m. Results at $t = 27$ and 33 h.

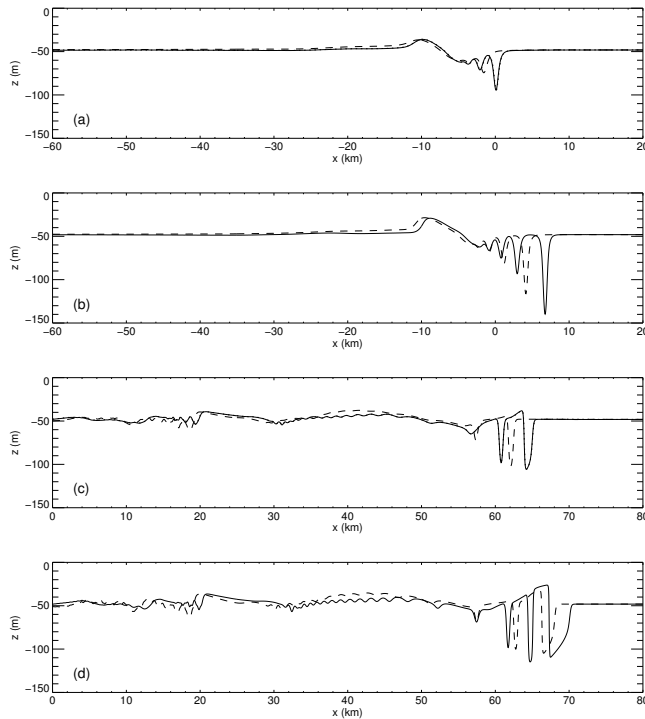


Figure 18. Effects of rotation are illustrated by comparing the $\sigma_t = 0.0232$ isopycnals for two different initial waves. Base stratification with bathymetry h_{15} . **(a, c)** Cases 3 and 3r: initial wave amplitude is 45.4 m ($\text{APE} = 100 \text{ MJ m}^{-1}$). **(b, c)** Cases 5 and 5r: initial wave amplitude is 71.6 m ($\text{APE} = 200 \text{ MJ m}^{-1}$). Solid curves are results without rotational effects. Dashed curve are results with $f = 5.35 \times 10^{-5} \text{ s}^{-1}$. Results are shown at times **(a, b)** $t = 23$ and **(c, d)** $t = 35$ h. The resolution for these results was $\Delta x = 33$ m and $J = 200$. Also plotted are results obtained using $\Delta x = 33$ and $J = 400$ for $f = 0$. These curves are indistinguishable from the lower resolution results.

Shoaling internal solitary waves

K. G. Lamb and
A. Warn-Varnas

Title Page

Abstract Introduction

Conclusions References

Tables Figures

◀ ▶

◀ ▶

Back Close

Full Screen / Esc

Printer-friendly Version

Interactive Discussion



Shoaling internal solitary waves

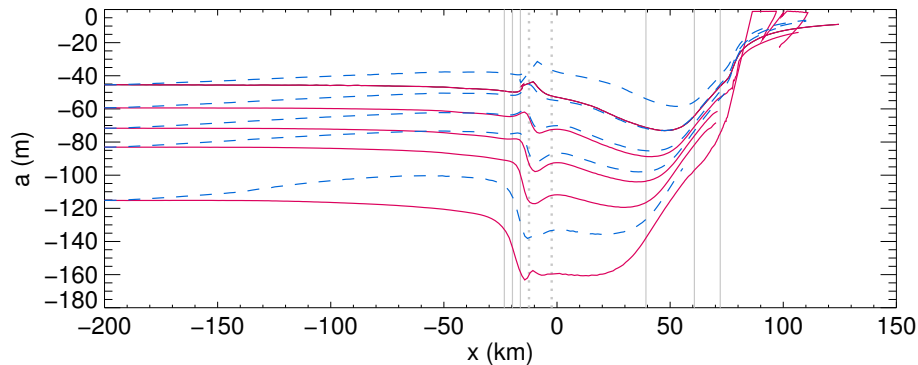
K. G. Lamb and
A. Warn-Varnas

Figure 19. Effects of rotation on the amplitude of the leading wave as a function of x . Bathymetry h_{15} . Solid red curves: cases without rotation. Dashed blue curves: cases with rotation. Cases 3–7 and 3r–7r. The solid vertical grey lines indicate locations where water depth is 1000, 800, 600 (first occurrence), 350, 200 and 120 m. The vertical dashed lines indicate the locations of the top of the bump at $x = -12.4$ km (480 m depth) and maximum depth (618 m) up shelf of it.

Title Page

Abstract

Introduction

Conclusions

References

Tables

Figures

◀

▶

◀

▶

Back

Close

Full Screen / Esc

Printer-friendly Version

Interactive Discussion



Shoaling internal solitary waves

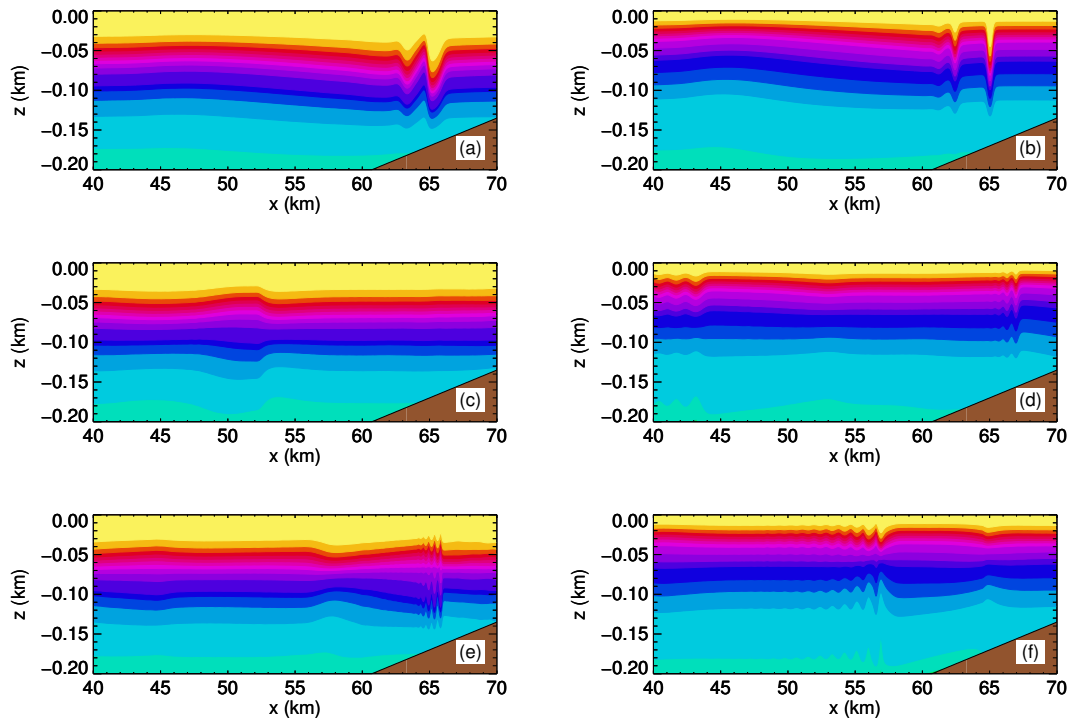
K. G. Lamb and
A. Warn-Varnas

Figure 20. Comparisons of wave fields using observed stratifications for $\text{APE} = 50 \text{ MJ m}^{-1}$ and bathymetry h_{15} . $f = 0$. **(a, c, e)** Case 8: density $\bar{\rho}_1$. **(b, d, f)** Case 11: density $\bar{\rho}_2$. **(a)** $t = 36 \text{ h}$. **(b)** $t = 38 \text{ h } 10 \text{ min}$. **(c, d)** $t = 47 \text{ h}$. **(e, f)** $t = 55 \text{ h}$.

Title Page

Abstract

Introduction

Conclusions

References

Tables

Figures

◀

▶

◀

▶

Back

Close

Full Screen / Esc

Printer-friendly Version

Interactive Discussion



Shoaling internal solitary waves

K. G. Lamb and
A. Warn-Varnas

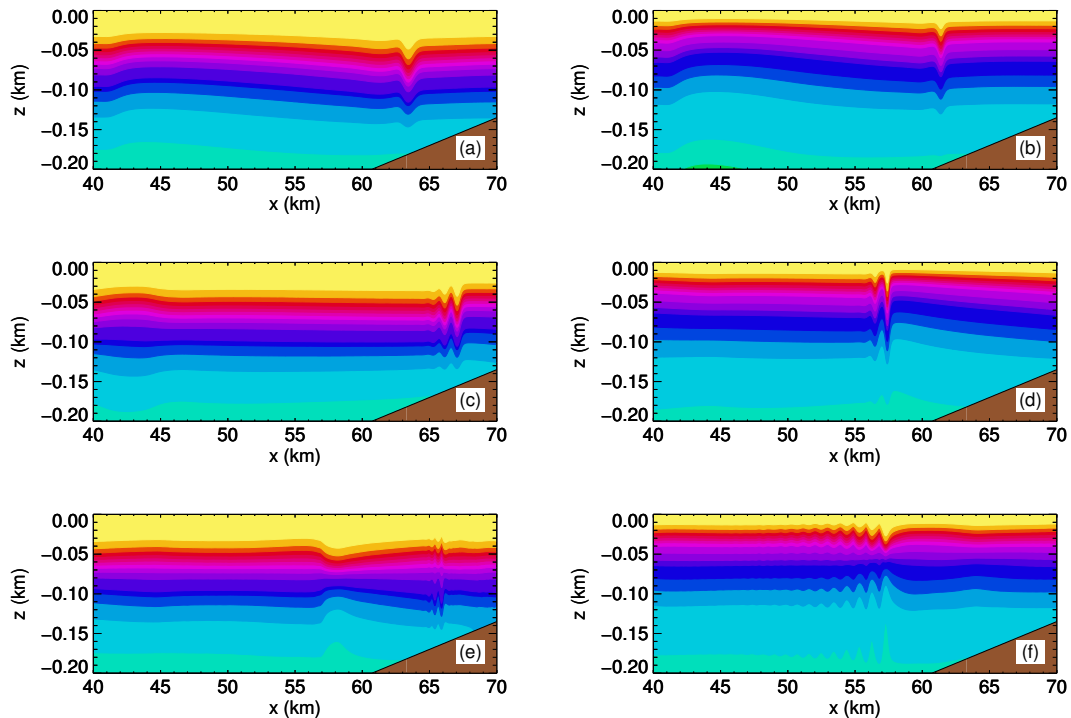


Figure 21. Same as previous figure but with $f = 5.33 \times 10^{-5} \text{ s}^{-1}$ (Cases 8r and 11r) and **(c, d)** are at $t = 43 \text{ h}$.

Title Page	
Abstract	Introduction
Conclusions	References
Tables	Figures
◀	▶
◀	▶
Back	Close
Full Screen / Esc	
Printer-friendly Version	
Interactive Discussion	



Shoaling internal solitary waves

K. G. Lamb and
A. Warn-Varnas

Title Page

Abstract

Introduction

Conclusions

References

Tables

Figures



Back

Close

Full Screen / Esc

Printer-friendly Version

Interactive Discussion

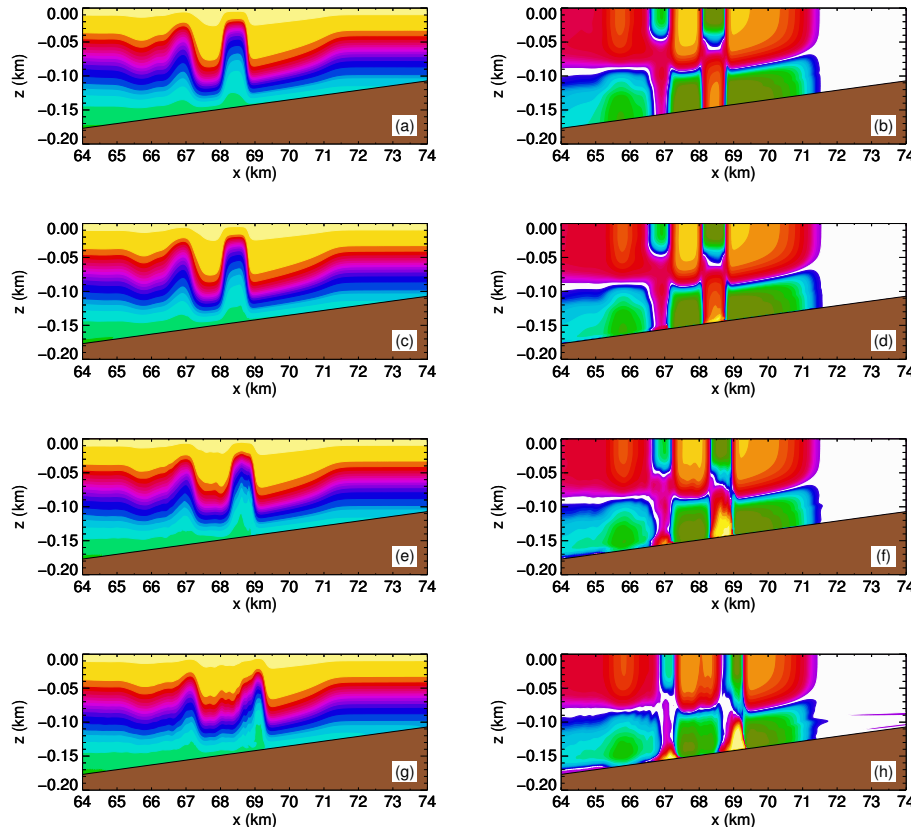


Figure 23. Effects of viscosity on shoaling waves. Stratification $\bar{\rho}_1$, initial wave amplitude 41.7 m ($APE = 100 \text{ MJ m}^{-1}$). Left panels show the density field, right panels show the horizontal velocities. For the velocity fields the red-orange-yellow colours indicate positive (on shelf) currents while green-blue indicate negative currents. **(a, b)** Inviscid. **(c, d)** $K = 1.0 \times 10^{-5} \text{ m}^2 \text{ s}^{-1}$. **(e, f)** $K = 1.0 \times 10^{-4} \text{ m}^2 \text{ s}^{-1}$. **(g, h)** $K = 1.0 \times 10^{-3} \text{ m}^2 \text{ s}^{-1}$.